DFT based microkinetic modeling of confinement driven [4+2] Diels-Alder reactions between ethene and isoprene in H-ZSM5

Journal Name

ARTICLE TYPE

DFT based microkinetic modeling of confinement driven [4+2] Diels-Alder reactions between ethene and isoprene in H-ZSM5[†]

Christopher Rzepa, Srinivas Rangarajan,[*]

We present a dispersion corrected periodic density functional theory investigation on the confinement driven catalysis of the [4+2] Diels-Alder cycloaddition reactions between ethene and isoprene by H-ZSM5. A detailed reaction network, which included competitive chemisorption and oligomerization of the reactants had been constructed; the reaction rates and product yields were inferred using microkinetic modeling. Our results show that the rates of Diels-Alder reactions were larger on the Brønsted acid sites of H-ZSM5 relative to their uncatalyzed reactions. This rate enhancement was driven by favorable dispersion interactions imparted by the framework on the transition states rather than their Brønsted-π interactions at the active site. A variance-based global sensitivity analysis showed that the formation of the C10 para-cycloadduct and its desorption, were both kinetically controlling and mathematically correlated. Ultimately, this led to a negative apparent order with respect to isoprene for the C7 cycloadduct, and fractional orders for the remaining C10 cycloadducts.

1 Introduction

One of the most successful advancements within the petro-chemical industry has been the application of zeolites, which are crystalline, alumino-silicate frameworks that consist of ordered, cage-like structures. Their utility arose from their distinct microporous topologies, which typically consist of subnanometer channels with various dimensionalities. Historically, they have been applied in the catalytic cracking of hydrocarbons[1] and light gas separations[2]; but have shown function in the conversion of methanol to olefins[3,4], Friedel-Crafts alkylation[5], Beckmann rearrangement[6], Fischer-Tropsch synthesis[7], among others.[8] To an extent, all of these processes are promoted by the principle of confinement; or how well the molecules fit within the zeolite's pores and active site. This concept suggests that the adsorbates conform to the curvature of the channel, becoming stabilized by maximizing their van der Waals interactions with the framework while limiting their entropic loss caused by transitioning from its unhindered ideal-gas state, and into the confines of the zeolite framework upon adsorption.[9] Consequently, confinement promulgates zeolites as molecular sieves, where prohibitively large species that cannot fit within their voids are excluded from adsorption and/or the reaction space. Likewise, smaller species

paired with large framework features may not incur any significant stability; and merely equilibrate with their bulk gas phase.[10] Optimal confinement occurs when the geometry of the reaction intermediates and/or transition states "match" their channel dimensions, acquiring enough stability to catalyze their respective reactions. For example, the rates of dimethyl ether carbonylation have been shown to be significant within zeolites containing eight-membered ring (8MR) channels, but were undetectable within zeolites containing 10+ MR channels exclusively.[11] Such specificity was attributed to the enthalpic stabilization of carbocationic transition states by the closer proximity of the surrounding framework's oxygen atoms within the 8 MR than 10+ MR channels. Yet configurations which maximize the adsorbate's van der Waals interactions with the framework (enthalpic stability) may not be preferred due to the entropic penalty incurred from the adsorbate's loss in mobility; and as a result, adsorbates have been shown to prefer non-intuitive arrangements within the zeolite channel. For example, high-temperature alkane activation reactions[11] have shown a preference toward 8-MR channels, but contain transition states too large to be fully encompassed within them. It was discovered that these transition states were only partially confined, extending the majority of their geometries into the adjacent 12 MR channel. Such "loose" configurations were preferred because they provided enough entropic freedom to exceed the enthalpic stability otherwise gained through complete adsorption within the 12 MR channels. Overstabilizing adsorbates is also possible, and has been shown to impede reaction rates through increased diffusion limitations[12,13], restrained product desorption,

---

Address, Department of Chemical and Biomolecular Engineering, Lehigh University, Bethlehem, PA 18015, USA.

[*] Corresponding Author: srr516@lehigh.edu

and increased intrinsic reaction barriers [14]. However confinement is not exclusive to zeolites; and has been shown to be a significant factor in catalyzing the oxidative dehydrogenation of hydrocarbons within mixed metal-oxides [15,16] and manganese oxide based octahedral molecular sieves [17], as well as catalyzing Diels-Alder reactions within macromolecules. [18] Understanding confinement is therefore a multifaceted problem; and despite our detailed understanding on an individual basis, our mechanistic understanding and ability to make empirical predictions remains limited.

In this work, we explore the effects of zeolite confinement on a set of Diels-Alder cycloaddition reactions. These reactions are an excellent archetype to study confinement because, 1) they can occur uncatalyzed, allowing for the effects of the zeolite framework to be separated from the reaction chemistry, and 2) their capability in producing cyclic regio-isomers provides a span of variously sized, but chemically identical, species. These reactions have been well studied and applied in the pharmaceutical, agro-chemical, and oleo-chemical industries for many decades. [19] Recently, tandem Diels-Alder-dehydration chemistries have been suggested for the synthesis of aromatic monomers from bio-mass based alternatives. [20] The [4 + 2] Diels Alder reaction, henceforth called "DA reaction", is particularly interesting because it forms a six-membered cyclic product (the cycloadduct) by coupling a 1,3-conjugated olefin (diene) with a double bonded moiety (dienophile). The cycloaddition reactions of such a diene + dienophile, followed by tandem dehydrogentation on a multifunctional catalyst, has been shown to result in valuable aromatic products. [21,22] At the core of this reaction, two π-bonds from the diene and one π-bond from the dienophile are broken, forming two new σ-bonds that enclose the product's six-membered ring as well a π-bond from the resulting electron rearrangement. This reaction typically occurs through a concerted mechanism, with the formation of the two σ-bonds occuring simultaneously through a single, pericyclic transition state. However, a stepwise mechanism is also possible, involving the formation of a diradical or zwitterionic intermediate. [23] Although they may be thermally driven to completion, the incorporation of homogeneous Lewis and Brønsted acids have been shown to not only catalyze these reactions, but also promote the selectivity of certain stereo and regio-isomers. [24–27] Zeolites are particular for this endeavor, because they offer Lewis/Brønsted acidity alongside confinement; which can limit undesirable byproducts or isomers and promote catalysis with particular selectivity. [10] Moreover, the preservation of regio-chemistry throughout the DA reaction allows one to control the bulkiness of the products and/or transition states. Meaning, a judicious choice between zeolite and reactants, whose products and/or transition state geometries appear to better fit within the channels, can be posited a-priori.

Despite being relatively unexplored, zeolites have been shown to catalyze DA reactions. However, the research has been largely focused on the DA cycloaddition between 2,5-dimethylfuran and ethene with subsequent dehydration to form xylenes; particularly due to the readily available synthesis of furans from bio-mass. [28] Williams et al. [29] have studied this reaction within zeolite HY, achieving a 75% selectivity toward para-xylene. Their findings suggest that the DA reactions occurred without a catalytic ac-

tive site; rather, the reaction was promoted by confinement and the role of the Brønsted acid site was instead attributed to the catalysis of the dehydration step. Nikbin et al. [21,30] have studied the application of HY and various alkali-exchanged Y zeolites for the same reaction using a combination of density functional theory and hybrid quantum mechanics/molecular mechanics calculations. Interestingly, their calculated DA activation barriers in HY were larger than their respective gas phase reactions, suggesting that they occurred uncatalyzed at the Brønsted active sites. Moreover, their results showed that alkali-exchanged Y zeolites (LiY, NaY, KY, RbY, CsY), in the form of Lewis acids, exhibited marginal catalytic activity toward DA reactions. On the contrary, the dehydration steps were shown to be significantly catalyzed at the Brønsted sites; and therefore they advocated that a bifunctional catalyst, one comprised of both Lewis and Brønsted acids, might better catalyze the overall process. Rohling et al. [14,31] have investigated the role of low-silica, alkali-exchanged Y zeolites (LiY, NaY, KY, RbY, CsY) on the same reaction using Density Functional Theory and microkinetic modeling. The scope of their work was to determine the collaborative effect of multiple cation sites on the DA cycloaddition/dehydration reactions against the standard, single site model. Their results suggest that low-silica alkali-exchanged Y zeolites are highly active catalysts for these reactions, owing to a combination of confinement-induced initial-state destabilization and transition state stabilization via ionic interactions with the collective alkali cations. In a subsequent work, Rohling et al. [32] have computationally investigated the catalytic effect of d-block cation exchanged high-silica Y zeolites on the DA cycloaddition step; and concluded that cations with less filled d-shell orbitals exhibited lower activation barriers. Apart from the familiar concerted single-step DA cycloaddition path; they also found a two-step path, which ultimately depended on the relative size of the cation. Other DA cycloaddition reactions have also been catalyzed by zeolites. For example, Bernardon et al. [33] have experimentally investigated DA reactions between isoprene and methyl-acrylate within different zeolite frameworks of various acid site densities. Among those frameworks, H-ZSM5 had the highest productivity and upwards of 91% selectivity toward the para- over the meta-cycloadduct. Ultimately, this catalytic effect was attributed to confinement. Apart from zeolites, macromolecules have also been shown to act as potential DA catalysts. Chakraborty et al. [18] have investigated the application of the macrocyclic molecule "cucurbit[7]uril" (CB[7]) as a catalyst for the DA reactions between benzene, furan, cyclopentadiene, and thiophene with ethene using Density Functional Theory. All reactions exhibited enhanced rate constants within the CB[7] molecule relative to their free state. However, the activation energy for each reaction was less favorable within CB[7] than their respective free state, suggesting that the activation entropy facilitated these reactions.

The objective of this work is to use periodic Density Functional Theory (DFT) based microkinetic modeling (MKM) to study the effects of confinement on the kinetics of the DA cycloaddition reactions between ethene (C2) and isoprene (C5) within H-ZSM5. The resulting DA cycloadducts are outlined within Figure 1, there is a single C7 product formed between isoprene and ethene (IU-
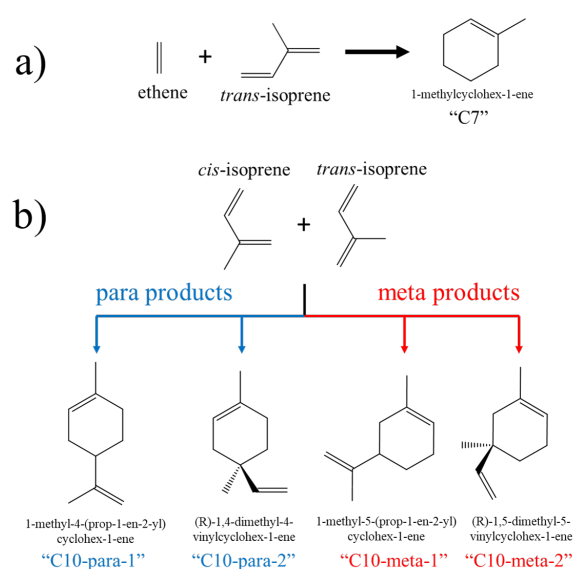
Fig. 1 The DA cycloaddition reactions between ethene and isoprene considered within this work. a) The DA cycloaddition reaction between ethene (diene) and *trans*-isoprene (dienophile) to form the C7 cycloadduct, IUPAC: "1-methylcyclohex-1-ene". b) The possible DA cycloaddition reactions between *cis*-isoprene (diene) and *trans*-isoprene (dienophile) to form four possible C10 cycloadducts. The cycloadducts were segregated based on their respective para- and meta- regiochemistries.
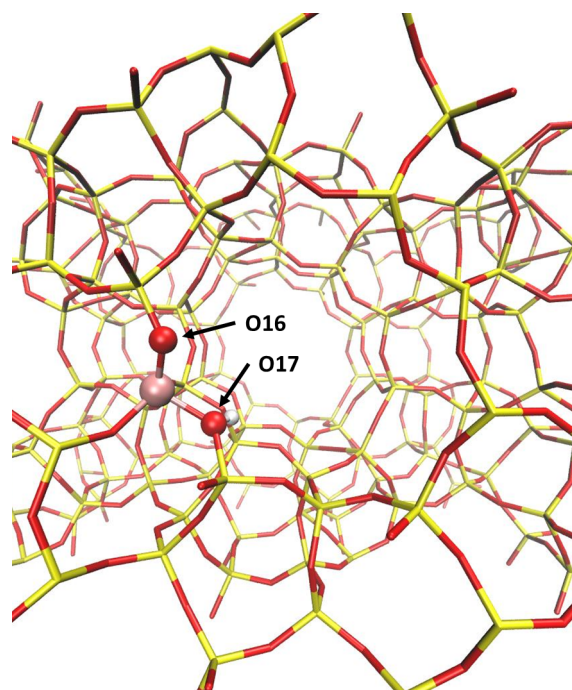

Fig. 2 The lone structure of H-[Al]ZSM-5, where the Brønsted proton is bound to O17 pointing along the straight channel toward an adjacent O17. The O16 oxygen is also emphasized. Key: silicon (yellow), oxygen (red), hydrogen (white), aluminum (pink).

PAC: "1-methylcyclohex-1-ene"); there are four C10 products that are formed from two isoprene molecules, and we have organized them by their "para-" and "meta-" regiochemistry. For brevity, we will be referring to the C10 products (and corresponding reactions) as "C10-para-1,2" and "C10-meta-1,2" with the exception of 1-methylcyclohex-1-ene which will be referred to as "C7". Our choice of reactants provides an array of variously shaped (meta- vs. para-) and sized (C7 vs. C10) transition states/products whose corresponding reactions can occur uncatalyzed. This allows us to gauge the extent of confinement relative to their uncatalyzed gas phase reactions; and infer discriminating factors based on the species size/shape. We have chosen to work with H-ZSM5 in view of its well studied applications as a catalyst for light olefin reactions [34–36], pervasive use in industry [1], and superiority in catalyzing similar DA reactions. [33]

The order of this paper is as follows: Section 2 describes our zeolite model and the methods incorporated into our DFT simulations, the approximations used in our thermodynamic corrections to the DFT energies, and kinetic derivation of our microkinetic model. In Section 3, we present a comparison of our adsorbed states against available literature, discuss our reaction pathways and compare them with competitive oligomerization and cyclization pathways. We also discuss the results of our microkinetic model and the global sensitivity analysis. In Section 4, we summarize the paper with concluding remarks.

2 Methods

The adsorption calculations have been simulated using one full periodic unit of the ZSM-5 orthorhombic structure taken from the International Zeolite Database (IZA). [37] The unit cell consisted of 192 Oxygen and 96 Silicon atoms with 12 distinguishable tetrahedral sites (T-sites); we follow the nomenclature of IZA to identify the T-sites. The Brønsted site was formed by substituting a single Si atom with Al and adding a hydrogen on the most stable adjacent oxygen. Based on the work of Ghorbanpour *et al.* [38], the T7 site was chosen as the Brønsted site; it was considered to be energetically favorable, providing good access due to its location at the intersection of the straight and sine channels. The effects of topologically identical locations on adsorption within the zeolite supercell were deemed negligible based on a prior work. [39]

All electronic structure calculations were performed using the Vienna ab initio simulation package (VASP) [40,41] through plane wave density functional theory (DFT). PAW potentials [42] with generalized gradient approximation (GGA) using the Perdew-Wang-Ernzerhof (PBE) [43] exchange correlation functional with Grimme-D2(DFT-D2) [44,45] dispersion corrections were used in view of its accuracy for small adsorbates in other zeolites. [39,46] The convergence criterion for electronic relaxation was 10^{-4} eV with a plane-wave energy cutoff of 400 eV; ionic convergence was set with the criteria that the force on each ion be smaller than 0.02 eV/Å. Gaussian smearing with width 0.1 eV was used; all energies were extrapolated to 0 K. Transition states were identified by using the climbing image nudge elastic band method (NEB) [47] with seven images between the reactants and product. The ionic convergence for the NEB calculations was set with the criteria that the force on each ion within each image be smaller than 0.1 eV/Å. As a consequence of the large unit cell size, the Brillouin zone was sampled using only the gamma point. Keep-

ing atoms constrained, optimization of the zeolite cell parameters resulted in: $(20.2 \times 19.9 \times 13.3$ Å$, \alpha, \beta, \gamma = 90°)$. Unadsorbed gas-phase calculations were performed at the same level of theory in a box that has at least 10 Å of vacuum between two images in any direction.

The enthalpies, entropies and Gibbs free energies for reactants, products, and transition states were derived using statistical thermodynamics. The harmonic normal mode approximation was used in determining the vibrational frequencies; for which the Hessian was calculated using finite difference implemented in VASP, with displacement steps of $\pm$ 0.015 Å and a convergence criterion of 10^{-6}eV. The zeolite framework was kept rigid in calculating the Hessian, with the exception of the Brønsted proton. The translational and rotational modes for the bulk-phase species were decoupled from the vibrational modes and their thermodynamic contributions were calculated according to the formal statistical thermodynamic treatment of an ideal gas. For adsorbed states, all imaginary and low-lying frequencies were replaced with a $100 cm^{-1}$ cutoff, based on a sensitivity analysis from a previous work.[46] The prevalence of imaginary frequencies for molecules adsorbed within zeolite frameworks under the harmonic oscillator approximation make it difficult to determine which, or if any such frequencies correspond to the transition state. One approach involves visualizing the displacement of atoms along the corresponding eigenvectors, which has been used to implement translational and rotational entropy corrections.[48,49] This approach was used in verifying our transition state structures, where each imaginary frequency was visualized and the mode corresponding to bond formation was discarded. The enthalpies were calculated by taking the sum of the DFT-calculated ground state electronic energy, the zero point vibrational energy, and temperature contributions from the constant pressure heat capacity, which was derive by fitting the entropy to a set of Shomate Parameters. Finally, the standard Gibbs Free Energy was derived from its classical definition of the enthalpy and entropy. (See equations 3 and 4 in SI.I of the Supporting Information.)

The thermodynamic quantities for adsorbed species were also calculated using this method, but were given in terms of an upper and lower bound based on approximations of the adsorbate entropy outlined in SI.I of the Supporting Information. The reality is that our thermodynamic adsorbate quantities fall somewhere between these two approximations[50,51]; we therefore report both values as bounds for our thermodynamic and kinetic parameters. Within this paper, these approximations are defined as "Free translator" and "Harmonic Oscillator" for the upper and lower entropic bounds respectively. We would like to emphasize that these approximations provide a lower and upper bound on the effect of channel size on the molecule's entropic freedom. Namely, the adsorbate is assumed to be unhindered in translating within an area commensurate to the zeolite cage size under the Free translator approximation, but completely immobile under the Harmonic Oscillator approximation. Empirically developed approximations for the adsorption of hydrocarbons on heterogeneous catalysts also exist. Namely, Campbell and Sellers[52] have developed a semi-empirical correlation for loosely-bound adsorbates on two-dimensional catalytic surfaces. Their correlation showed a standard deviation of only 2.2R for the adsorbate entropy over a range of 50R. Likewise, Dauenhauer and Abdelrahman[53] have also developed a semi-empirical correlation for the adsorption of hydrocarbons within various acidic zeolites. A comparison among the Harmonic Oscillator, Free Translator, Campbell and Sellers's correlation, and Dauenhauer and Abdelrahman's correlation for the reactants and products considered within this study can be found within Table S1 of the Supporting Information. We have decided to only consider the Harmonic Oscillator and Free Translator approximations within this study because: 1) the Campbell and Sellers approximation is particular for two-dimensional catalytic surfaces, and 2) the Dauenhauer and Abdelrahman approximation was developed without any of the reactants and products considered within this study. Additionally, the Free Translator has shown to be competent in predicting the entropy of C2-C8 alkanes/alkenes and cyclic species.[50,54-57]

Adsorption/desorption steps were constructed by forming pseudo-transition states which have the entropy of their corresponding adsorbate under the Free Translator approximation, and the enthalpy of their ideal-gas state, this derivation and rationale is outlined within SI.II of the Supporting Information. The derivation of our MKM and relative analyses (conversion, selectivity, yield, apparent activation energy, apparent reaction order) can also be found in SI.III of the Supporting Information.

3 Results and Discussion

3.1 Reactant adsorption

We begin our analysis by validating the adsorption of our stable intermediates at standard conditions against available results. Table 1 shows our reactant DFT energy, enthalpy, entropy, and Gibbs free energy change upon adsorption at standard conditions (298.15 K and 1 atm). Adsorption was defined by equation 1, where "X" represents the thermodynamic quantity of interest and the subscripts $molecule^*$, $molecule_{(g)}$, $Zeolite$, represent the adsorbed, gas and lone zeolite states respectively. Due to the propensity of olefins to undergo oligomerization reactions within acidic zeolites (see section 3.3), we have investigated three possible scenarios for the adsorption of each reactant: 1) A physisorbed π-complex, where the Brønsted proton is interacting with the olefin but no distinct bond is formed; 2) Protonation of the olefin, resulting in the formation of a covalent alkoxide bond with an oxygen atom at the acid site; 3) Protonation of the olefin, resulting in a stable carbenium ion. Theoretically, protonation may occur on any of the carbon atoms involved in its π-bonds. Moreover, the Brønsted proton at the acid site has been shown to be mobile, capable of migrating among adjacent oxygen atoms.[58] As a result, the alkoxide bond may theoretically be formed with any of the adjacent framework oxygen atoms. We have examined each of these possibilities, but only the most favorable states are discussed here.

$$\Delta X_{adsorption} = X_{molecule^*} - X_{molecule_{(g)}} - X_{Zeolite} \qquad (1)$$
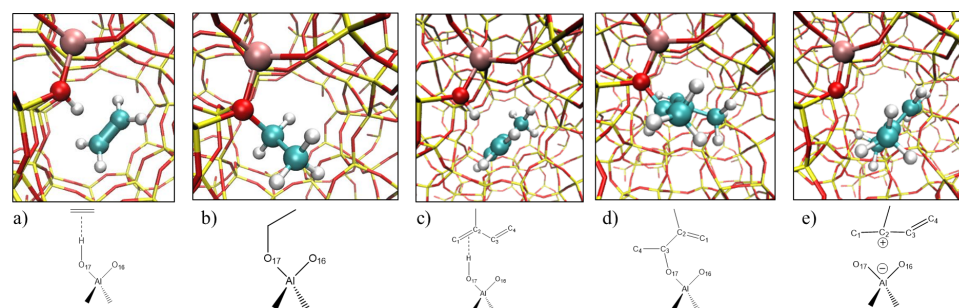
Fig. 3 The most energetically stable adsorption configurations of our reactants. The Brønsted proton is bound to O17 for each image; and the aluminum, proton, and oxygen (O17) were emphasized using spheres. The reactant atoms were also represented as spheres, with double bonds emphasized using thicker diameters. Key: silicon (yellow), oxygen (red), hydrogen (white), aluminum (pink), carbon (turquoise) a) Ethene physisorption, where there is a distinct interaction between the Brønsted proton and ethene's double bond. b) Ethene chemisorption, where the primary carbon has been protonated; and an alkoxide bond has formed between O17 and the remaining carbon. c) *Trans*-isoprene physisorption, where the Brønsted proton at the acid site is interacting with the double bond between the primary and tertiary carbons. d) Isoprene chemisorption, where the primary carbon "C_4" has been protonated and an alkoxide bond has formed between the tertiary carbon "C_3"" and O17. e) Carbenium isoprene chemisorption, where the tertiary carbon "C_3" has been protonated.

	Adsorbate	ΔE [(kJ/mol)]	ΔH^0 [(kJ/mol)]	ΔS^0 [J/mol/K]	ΔG^0 [(kJ/mol)]
physisorbed	ethylene	-63	-58(-59)	-143(-107)	-15(-27)
	trans-isoprene	-100	-96(-98)	-191(-147)	-39(-54)
alkoxide	ethene	-108	-96	-171	-45
	isoprene	-90	-80	-208	-18
carbenium	isoprene	-70	-67(-68)	-179(-136)	-13(-27)

Table 1 Standard enthalpy (kJ/mol), entropy ($J/mol/K$), and Gibbs free energy (kJ/mol) of adsorption at 298.15 (K) and 1 (atm) with the Free Translator approximation quantities housed within parenthesis

3.1.1 Ethene

Our relaxed complex for the physisorbed state of ethene is shown in Figure 3 a). Consistent with other works[46,48], the Brønsted proton is attracted to the center of the π-bond of ethene. The formation of this physisorbed structure is exergonic, with a Gibbs free energy of -15(-27)(kJ/mol). The most favorable chemisorbed structure of ethene is shown in Figure 3 b), with the alkoxide bond formed with oxygen O17 (also the most stable oxygen for the Brønsted site). The chemisorption of ethene was found to be more favorable by -18(-30) (kJ/mol) than physisorption, with a Gibbs Free Energy of -45 (kJ/mol). No stable carbenium ion was found for ethene, which is consistent with other works which suggest that small olefins exist as carbeniums only through transition states during chemisorption.[59,60]

Nguyen *et al.*[48] have computationally investigated the adsorption of C2-C8 linear alkenes in various acidic zeolites at the QM-Pot(MP2//B3LYP:GULP) level of theory. Specifically, they have calculated the standard enthalpy, entropy, and Gibbs free energy change for the physisorption, chemisorption and protonation of ethene within H-ZSM5. Their calculated Gibbs free energy of ethene physisorption was -20 (kJ/mol), which falls within our range of -15(-27) (kJ/mol). Their entropy and enthalpy are also consistent with our values. On the other hand, their Gibbs free energy of chemisorption was -69 (kJ/mol), approximately 24 (kJ/mol) more negative than our value. A direct comparison between our chemisorption energies shows that DFT-D2 dispersion corrections predict a more positive binding energy by 22 (kJ/mol).

In a separate study[46], we assessed the interactions between the π-bond of ethene with the active sites of Brønsted and cation exchanged ZSM-5 zeolites by measuring its heat of adsorption using microcalorimetry and periodic DFT calculations at low temperature. As a comparison, the adsorption of ethane was also quantified, given its lack of a π-bond but otherwise similar physical properties to ethene. While both adsorbates showed identical experimental heats of adsorption within siliceous ZSM-5, ethene showed a significantly stronger adsorption within H-ZSM5 (8 (kJ/mol)) than the adsorption of ethane (2 (kJ/mol)). These results suggest that while ethene and ethane share similar confinement effects, ethene exhibits additional Brønsted-π interactions at the active sites within H-ZSM5. The PBE(DFT-D2) functional correctly captured this enhanced stability of ethene, but predicted a value 20 (kJ/mol) more negative relative to experiment. A comparison among different DFT functionals (Grimme-D2[44,45], Grimme-D3[45], Tkatchenko-Scheffler[61], DDsC[62,63], vdw-Df(2)[64–66]) for this system showed a wide variation in the binding energies of ethene/ethane (almost 32 (kJ/mol)), but all correctly captured that ethene interacts more strongly than ethane at the Brønsted acid site. Accordingly, while our DFT calculations may overpredict experimental values, we expect our model to correctly capture qualitative differences.

3.1.2 Isoprene

Our relaxed physisorbed complex of isoprene is shown in Figure 3 c). The Brønsted proton resides on O17; and is directed toward the center of the π-bond between the primary and tertiary carbons (labelled as "C_1" and "C_2" within Figure 3 c) respectively). This configuration is consistent with other physisorbed olefins of similar size within acidic zeolites. [48,67–69] The adsorption was exergonic, with a Gibbs free energy of -39(-54)(kJ/mol).

The most stable chemisorbed state of isoprene is shown in Figure 3 d), where the primary carbon "C_4" has been protonated; and an alkoxide bond formed between the secondary "C_3" carbon with the host oxygen O17. The Gibbs free energy of this chemisorbed state was -18 (kJ/mol). Unlike ethene, we have found a stable tertiary-carbenium ion; and its relaxed structure is shown in Figure 3 e). Adsorption of this tertiary-carbenium was also found to be exergonic, with a Gibbs free Energy of -13(-27) (kJ/mol). The resulting alkoxides from this tertiary-carbenium were found to be very energetically unfavorable. (See Figure 8 of Section 3.3) Ultimately, the physisorbed state of isoprene was found to be more thermodynamically favorable than the chemisorbed and carbenium states by 12(40) (kJ/mol) and 26(25) (kJ/mol) respectively.

Nguyen et al. [68] have looked into the physisorption, chemisorption, and protonation of isobutene in various acidic zeolites using periodic density functional theory at the PW91-D//PW91 level of theory. On the basis of their calculations, the standard Gibbs free energy of formation for physisorbed isobutene within H-ZSM-5 is slightly more stable than its tertiary-butyl carbenium ion, but significantly more stable than its chemisorbed counterparts.

Moreover, Cnudde et al. [70] have computationally studied the temperature dependent stability of C4-C5 alkene cracking intermediates within H-ZSM-5 using ab-initio and molecular dynamics simulations. The results of their static simulations (non MD) have shown that physisorption is more stable than chemisorption, regardless of the alkene (branched vs. linear) or temperature (323-773 K). Their dynamic simulations (MD) at 323 K showed systemic deprotonation for linear carbenium species, whilst the physisorbed and alkoxide species remained stable. However the MD simulations of branched intermediates have shown that the physisorbed and chemisorbed species experienced prompt protonation into stable carbenium ions.

These studies are somewhat consistent with our results, because we have found that the physisorbed complex of isoprene is more stable than its chemisorbed and carbenium counterparts. However, our tertiary-carbenium state is only "significantly" more stable than chemisorbed isoprene if we assume our entropy approximation is more accurately described by the Free Translator. While MD simulations to analyze the stability of isoprene adsorption are outside the scope of this paper, we postulate that the range of our thermodynamic approximations encompasses the stability of these higher free energy states.

3.2 Diels-Alder product adsorption

The most stable configurations of our adsorbed DA products are shown in Figure 4; and their respective DFT energy, enthalpy, entropy, and Gibbs Free energy change upon adsorption (defined by equation 1) at 298.15 K and 1 atm are given in table 2. Synonymous with the configurations of the physisorbed reactants, each product exhibited an interaction between the Brønsted proton on O17 with one of its π-bonds. For the C7 product this interaction occurred with its lone π-bond; but for the C10 products, it was observed with either the π-bond of the dienophile (external to the six-membered ring) or with the π-bond of the diene (internal to the six-membered ring). The C10-meta products preferred this interaction with their external π-bond, while the C10-para products preferred to interact with their internal π-bonds. The Gibbs free energy of adsorption for the C10-para products were on average 8 (kJ/mol) more favorable than the C10-meta products, with the C10-para2 product being most strongly adsorbed by an average of 14 (kJ/mol).

3.3 Reaction pathways

The adsorption of small olefins at the Brønsted acid sites of zeolites have a propensity to oligomerize at temperatures as low as 300 K. [71–76] At higher temperatures, these oligomers have been shown to further undergo cyclization reactions, which can subsequently dehydrogenate to form a myriad of cyclic products. [77,78] In particular, our C7 product may be formed via the 1,6 ring closure/dehydrogenation of a primary alkoxide, formed by the oligomerization between isoprene and ethene (see Figure 5). The extent that these reactions may compete with DA cycloaddition is otherwise unknown; but Bernardon et al. [33] have run similar DA reactions (isoprene with methyl-acrylate) within H-ZSM5 at temperatures between 293.15 to 363.15 K without appreciable formation of such byproducts. The conditions for our reaction were chosen to be 368.15 K and 1 atm. Our choice of a slightly larger temperature than Bernardon et al. was based on the results of our MKM (Discussed in Section 3.4), whereby we found that the DA reaction rates within the zeolite at this temperature were $\approx 33x$ higher than in gas phase while likely suppressing side reactions. (See Figure S7 of the Supporting Information).

3.3.1 Diels-Alder cycloaddition

Figure 6 displays the Gibbs free energy surface of our adsorbed and gas-phase DA reactions at 368.15 K and 1 atm; with corresponding barriers given in Table 3. The primary and most important observation is that the Gibbs free energy difference for each adsorbed DA TST with respect to the unadsorbed gas-phase reactants "ΔG_{rel}" is substantially smaller than their corresponding gas-phase barriers "$\Delta G_{af(g)}$", suggesting that these reactions are catalyzed within H-ZSM5. All DA reactions showed an average 37(56) (kJ/mol) lower ΔG_{rel} relative to their unadsorbed gas-phase barriers. The ΔG_{rel} for the C7 reaction was on average 7(5) (kJ/mol) smaller relative to the other DA reactions, but its unadsorbed gas-phase barrier was 26 (kJ/mol) smaller among the unadsorbed gas-phase reactions. The C10 reactions showed a more significant change in their ΔG_{rel} relative to their corresponding unadsorbed gas-phase reactions, being on average 46(66) (kJ/mol) and 35(55) (kJ/mol) lower for the meta and para product regio-isomers respectively (with C7 being only 22(40) (kJ/mol) lower). Among the C10 reactions, both meta
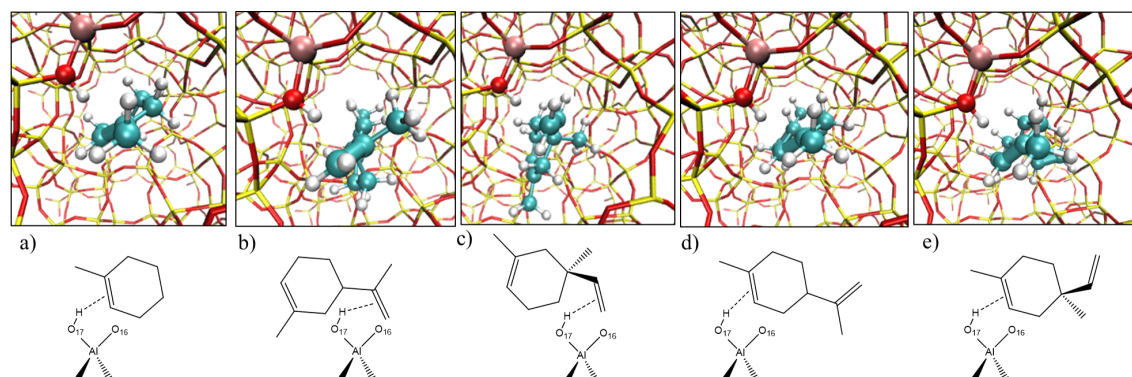
Fig. 4 The most energetically stable adsorption configurations of our Diels-Alder products. The Brønsted proton is bound to O17 for each image; and the aluminum, proton, and oxygen (O17) were emphasized using spheres. The reactant atoms were also represented as spheres, with double bonds emphasized using thicker diameters. Key: silicon (yellow), oxygen (red), hydrogen (white), aluminum (pink), carbon (turquoise) a) Product C7 physisorption, where the Brønsted proton interacts with C7's double bond. b) Product C10-meta1 physisorption, where the Brønsted proton interacts with C10-meta1's external double bond. c) Product C10-meta2 physisorption, where the Brønsted proton interacts with C10-meta2's external double bond. d) Product C10-para1 physisorption, where the Brønsted proton interacts with C10-para1's internal double bond. e) Product C10-para2 physisorption, where the Brønsted proton interacts with C10-para2's internal double bond.

adsorbate	ΔE [(kJ/mol)]	ΔH^0 [(kJ/mol)]	ΔS^0 [J/mol/K]	ΔG^0 [(kJ/mol)]
$C7$	-127	-121(-123)	-203(-157)	-61(-76)
$C10 - para1$	-146	-138(-140)	-224(-175)	-71(-88)
$C10 - para2$	-155	-150(-151)	-218(-169)	-85(-101)
$C10 - meta1$	-141	-135(-136)	-226(-177)	-67(-83)
$C10 - meta2$	-145	-138(-140)	-218(-169)	-73(-89)

Table 2 Standard enthalpy (kJ/mol), entropy ($J/mol/K$), and Gibbs free energy (kJ/mol) of adsortpion at 298.15 (K). The lower and upper bounds are given by the harmonic and Free Translator approximations defined in section SI.I of the Supporting Information, with the Free Translator quantities housed within parenthesis
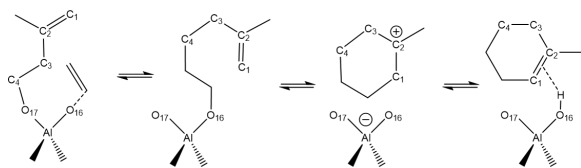

Fig. 5 Proposed mechanism for the oligomerization of primary isoprene alkoxide with ethene, with subsequent cyclization and dehydrogenation to form product C7.

Reaction	ΔG_{af} [(kJ/mol)]	ΔG_{rel} [(kJ/mol)]	$\Delta G_{af(g)}$ [(kJ/mol)]
$C7$	80(79)	66(48)	88
$C10 - para1$	91(89)	78(59)	110
$C10 - para2$	90(88)	77(57)	115
$C10 - meta1$	83(81)	70(50)	115
$C10 - meta2$	81(79)	68(49)	115

Table 3 The intrinsic Gibbs free energy barrier "G_{af}" (difference between the TST and reactants within the adsorbed phase), the relative Gibbs free energy difference between the adsorbed TST and unadsorbed reactants "G_{rel}", and unadsorbed gas-phase barriers for the DA reactions "$G_{af(g)}$", as illustrated in Figure 6 at 368.15 K and 1 atm.

regio-isomers exhibited lower ΔG_{rel} by 9 (kJ/mol) relative to the ΔG_{rel} of the para regio-isomers. Because the entropic approximations are largely cancelled when comparing among these reactions, we attribute such stability differences to the DFT energies. Therefore, our data show: 1) The larger C10 TSTs are more stabilized by the framework than the C7 TST, and 2) The meta regio-isomers are more stabilized by the framework than the para regio-isomers, relative to their uncatalyzed gas-phase reactions.

The TST configurations corresponding to our DA reactions are shown in Figure 7 and in all cases it was found that the most energetically stable configurations preferred cis-isoprene (the diene) to reside at the acid site. These structures largely resemble their co-adsorbed states rather than their products, which was also observed in the gas-phase (see Figure S5 of the Supporting Information). Unlike the configurations of the adsorbed products shown in Figure 4, the Brønsted proton preferred to interact more

closely with one of the carbon atoms involved in a π-bond rather than the π-bond itself. In particular, the Brønsted proton preferred to interact with the secondary carbon of the cis-isoprene (diene) for the C7 TST, represented within Figure 7 a). However, for the C10 TSTs, this interaction ranged between the primary and tertiary carbon atoms of the cis-isoprene (diene), ultimately depending on whether the final product was para or meta. The C10-para TSTs are represented within Figure 7 b) and c); and it can been seen that the Brønsted proton preferred to interact with the tertiary carbon. However, for the C10-meta TSTs (represented within Figure 7 d) and e)), the Brønsted proton preferred to interact with the primary carbon.
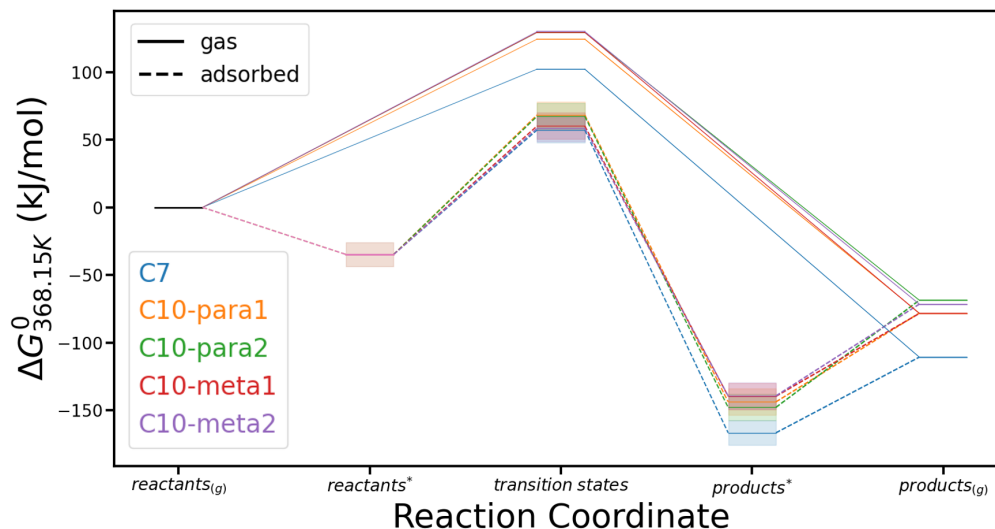
Fig. 6 The Gibbs free energy surface of our adsorbed (dashed line) and gas (solid line) DA reactions at 368.15 (K). The conditions for our reaction were based on the results of our MKM (Discussed in Section 3.4). The x-axis represents the reaction coordinate, which is segregated between the adsorbed and gas states; represented by "*" and "(g)" super/subscripts respectively. All path energies have been normalized relative to their respective gas-phase reactants. The adsorbed reactants are non-interacting and their energies were taken as the sum of their most stable physisorbed configurations from Table 1 with their corresponding secondary reactant from the bulk gas phase. The product energies were taken from their most stable configurations outlined in Table 2. The shaded regions represent the thermodynamic limits defined by the harmonic and Free Translator approximations, with each state representing an average between those two limits.)

3.3.2 Competitive chemisorption and cyclization pathways

Historically, two pathways for olefin oligomerization have been considered: 1) a concerted mechanism in which protonation and C-C coupling occur simultaneously, or 2) a step-wise mechanism, where protonation results in the formation of an intermediate alkoxide before coupling with an additional olefin. Svelle et al.[79] have investigated both pathways using DFT in the dimerization of linear alkenes; but the prevailing pathway was inconclusive. On the other hand, Shen W.[80] have concluded that while the concerted mechanism for ethene dimerization is preferred in large pore zeolites, both pathways are competitive for smaller pore zeolites (i.e H-ZSM5). Without claiming exclusivity, we have investigated the step-wise mechanism; which has been predominantly chosen in works concerning olefin cyclization and β-scission.[75,77,81]

Unlike oligomerization, the mechanism for olefin chemisorption is well established, and is illustrated within Figure 8.[48,67,68,75,76] The path begins with a physisorbed complex, where the Brønsted proton interacts with the π-bond of the olefin. Chemisorption is initiated by protonation of either π-bonded carbon in the olefin, ultimately traversing through a cationic TST before forming a covalent alkoxide bond with the adjacent oxygen atom in the framework. The rate of this step has been shown to depend upon the stabilization of this cationic TST, with tertiary carbons preferring to house the positive charge over secondary or primary carbons.[48,68] However, protonation of olefins containing tertiary carbons (i.e isoprene) have been found to form stable carbenium intermediates in the form of physisorbed carbocationic states. For example, Ngueyn et al.[68] have shown tert-butyl car-

beniums to be more stable than their alkoxide analogs at temperatures as low as 300 K.[68]

In Figure 9 we show the Gibbs free energy surface for the physisorption, protonation, and subsequent chemisorption of ethene and isoprene at 368.15 K and 1 atm. Although we have considered many possible adsorption configurations at these conditions, the most thermodynamically favourable states remained those discussed within section 3.1. In particular, the Brønsted proton preferred to reside at O17, being 10 (kJ/mol) more stable than at O16. Physisorbed ethene and *trans*-isoprene continued to be preferred at O17 than O16 by 16 and 19 (kJ/mol) respectively. In their chemisorbed states, both ethene and isoprene preferred to form their alkoxide bond with O17 rather than O16 by 39 and 19 (kJ/mol) respectively. Stable carbenium intermediates were only found for isoprene, with protonation occurring on the primary carbon such that either a secondary or tertiary carbenium ion was formed. The tertiary carbenium was found to be 15 (kJ/mol) more stable than the secondary carbenium, however the subsequent tertiary alkoxide was 15 (kJ/mol) less stable than the secondary alkoxide. Overall, the two most thermodynamically favorable adsorption configurations; and therefore most likely to occupy the acid site, were: 1) *trans*-isoprene physisorbed at O17, and 2) chemisorbed ethene at O17. The favourablity between these two states depended upon the thermodynamic approximation used. In particular, physisorbed *trans*-isoprene can be 10 (kJ/mol) more favorable (Free Translator), or 7 (kJ/mol) less favourable (harmonic oscillator) than chemisorbed ethene. Despite being thermodynamically similar at these conditions, the physisorption of *trans*-isoprene was found to be the kinetically favored adsorbate.
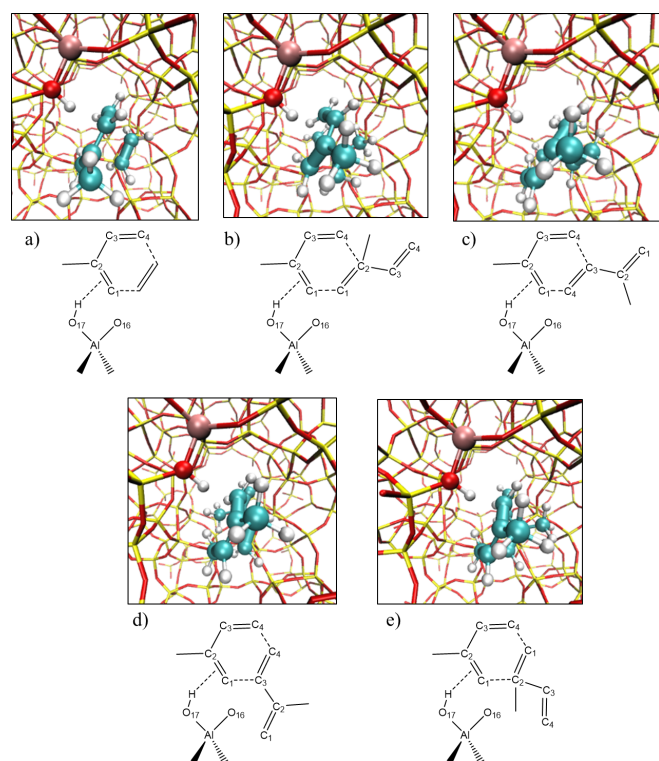
Fig. 7 The most energetically stable adsorption configurations of our Diels-Alder transition states (TST). The Brønsted proton is bound to O17 for each image; and the aluminum, proton, and oxygen (O17) were emphasized using spheres. The reactant atoms were also represented as spheres, with double bonds emphasized using thicker diameters. Key: silicon (yellow), oxygen (red), hydrogen (white), aluminum (pink), carbon (turquoise) a) Product C7 TST, where the Brønsted proton interacts with the diene's secondary carbon "C_2". b) Product C10-para2 TST, where the Brønsted proton interacts with the tertiary carbon "C_2" on the diene. c) Product C10-para1 TST, where the Brønsted proton interacts with the tertiary carbon on the diene. d) Product C10-meta1 TST, where the Brønsted proton interacts with the diene's primary carbon "C_1". e) Product C10-meta2 TST, where the Brønsted proton interacts with the diene's primary carbon "C_1".
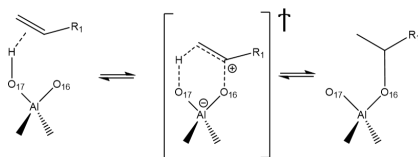

Fig. 8 General mechanism for olefin chemisorption at a zeolite's Brønsted site. The formation of the alkoxide bond is formed with an adjacent framework oxygen.

The minimum energy path for chemisorption occurs through the formation of a covalent alkoxide bond with an adjacent oxygen atom at the acid site. Therefore, the path for ethene chemisorption at O17 requires: 1) an initial proton migration between O17 to O16, 2) physisorption of ethene at O16, and 3) protonation of ethene with chemisorption at O17. The Gibbs free energy surface for this mechanism is represented by the pink colored path in Figure 9. The barrier for the proton to migrate from O17 to O16 is represented by the path connecting states "0" to "1" in Figure 9; it had an electronic DFT barrier of 69 (kJ/mol) and a Gibbs free energy barrier of 58 (kJ/mol). Sierka and Sauer have also investigated proton mobility in ZSM-5 by performing QM-POT calculations at the CCSD(T) level of theory.[82] Likewise, they considered the T7 O17 Brønsted site as the most energetically stable (labeled as O7 within their paper); and found the electronic barrier for proton migration to be 80.7 (kJ/mol), approximately 12 (kJ/mol) more positive than our predictions. Upon physisorption of ethene at O16, the barrier for protonation is represented by the path connecting states "5" to "4" within Figure 9. For this step, both the intrinsic Gibbs free energy and electronic DFT barriers were 64 (kJ/mol). Early ab-initio calculations using general zeolite models have shown intrinsic barriers for ethene chemisorption to be between 68-129 (kJ/mol).[83–85] More recently, Shen W.[80] and Chu et al.[86] have seperately investigated ethene dimerization within H-ZSM5 using DFT methods on variously sized cluster models. Both models had the aluminum atom located at the T12 position and the Brønsted proton residing at O24. Shen W. found the intrinsic energy barrier for the chemisorption of ethene from the physisorbed state to be 70-98 (kJ/mol); while Chu et al. have found barriers between 68-80 (kJ/mol). Work by Gleeson D.[87] using DFT based cluster models calculated an instrinsic barrier between 78-119 (kJ/mol). Based on these results, our calculated intrinsic barrier of 64 (kJ/mol) was slightly underpredicted. Nevertheless, our underprediction reinforces that ethene chemisorption will be kinetically limited relative to *trans*-isoprene physisorption.

Given its small chemisorption barriers (relative to DA cycloaddition) and occupancy at the Brønsted site, we expect rapid equilibriation of *trans*-isoprene among its protonated states. As such, we reckon with a possible cyclization/dehydrogenation pathway for the formation of our C7 product. We based our mechanism on a low-energy route proposed for the cyclization between ethene and propene by Vandichel et al.;[77] which consisted of: 1) chain growth through oligomerization between a chemisorbed olefin with a co-physisorbed olefin, 2) cyclization of the formed chain. The necessary chain to undergo cylization into our C7 product may only be generated through the oligomerization between a primary isoprene alkoxide with co-adsorbed ethene. This primary alkoxide is formed by the initial protonation of the secondary carbon of isoprene "C_3"; with the alkoxide bond formed between the primary "C_4" carbon of isoprene with the framework oxygen O16. We have found two transition states and a stable cationic cyclopropyl intermediate along this path (see Figure 10). Although stable cyclopropane intermediates have been found in steps such as ethene methylation[72] and skeletal isomerization of alkenes[88,89], their cationic forms have only been predicted as TSTs preceding
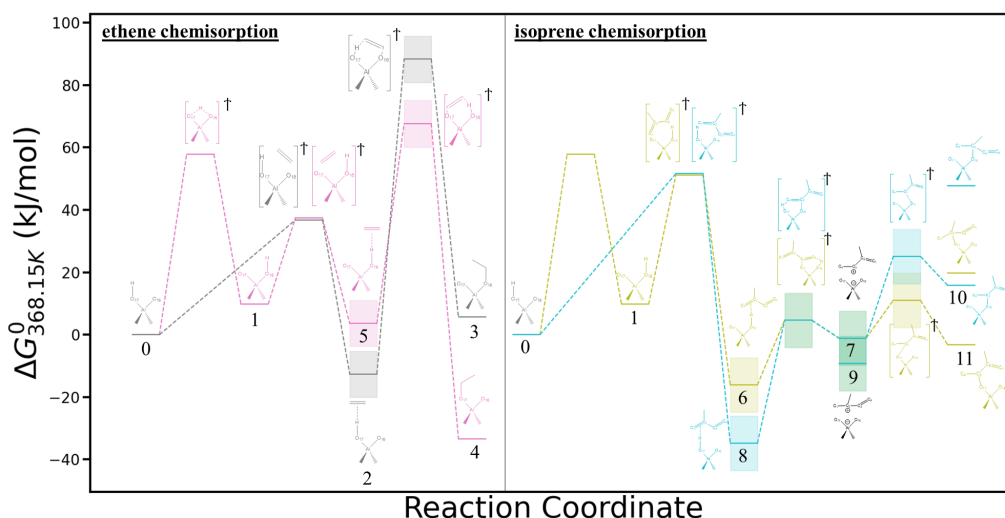
Fig. 9 The Gibbs free energy surface at 368.15 K and 1 atm of the physisorption and subsequent chemisorption of ethene (Left) and isoprene (Right). The grey and turquoise path show olefin physisorption at O17 with chemisorption occurring at O16 for ethene and *trans*-isoprene respectively. The pink and olive paths show proton migration form O17 to O16 followed by physisorption of the olefin at O16 with subsequent chemisorption at O17 for ethene and *trans*-isoprene respectively. The numbering scheme for each state is as follows: 0) Brønsted site at O17, 1) Brønsted site at O16, 2) physisorbed ethene at O17, 3) chemisorbed ethene at O16, 4) chemisorbed ethene at O17, 5)physisorbed ethene at O16, 6) physisorbed *trans*-isoprene at O16, 7) secondary carbenium isoprene, 8) physisorbed *trans*-isoprene, 9) tertiary carbenium isoprene, 10) secondary alkoxide isoprene at O16, 11 secondary alkoxide isoprene at O17. Only the most stable physisorbed/chemisorbed states were shown, with the exception of tertiary isoprene alkoxides whose states are not connected, but are listed above states 10 and 11. The shaded regions represent the thermodynamic limits defined by the harmonic and Free Translator approximations, with the state representing an average between those two limits. The "†" superscript represents TSTs.

ring closure or isomerization. However, such TSTs were not larger than di-methyl-cyclopropane and we rationalize the stability of our intermediate through the additional hydrogen bonding with the framework from its larger carbon number (C7 vs. C5).

The Gibbs free energy surface at our nominal conditions for the oligomerization/cyclization pathway to form our C7 product is shown in Figure 10. For comparison, we have also included the DA cycloaddition barrier, beginning with physisorbed *trans*-isoprene. It is evident, by Figure 10, that the DA cycloaddition barrier is not only kinetically favored; but is also thermodynamically preferred. In particular, the oligomeric intermediates along the cyclization path are almost equivalently less stable than physisorbed *trans*-isoprene, while the barriers for TST1 and TST2 with respect to physisorbed *trans*-isoprene are larger than DA cycloaddition. Based on these results we conclude that the DA cycloaddition is the dominant path toward C7 formation; and have disregarded the competitive oligomerization/cyclization pathway from our MKM.

3.4 Microkinetic modeling and sensitivity analysis

We begin our analysis by first comparing our DFT based MKM against experimental results for a similar reaction. Apart from furan chemistry, zeolite catalyzed DA reactions have been relatively unexplored. The most comparable experiment is that reported by Bernardon et al.[33], who investigated DA reactions between isoprene (diene) and methyl-acrylate (dienophile) within many acidic zeolites at 348.15 K and 1 atm. They have concluded that H-ZSM5 zeolites had the highest activity for DA reactions, achieving site time yields (STY) between 0.05-0.219 ($mmol - product/mmol - H + /hour$) toward their most selective product
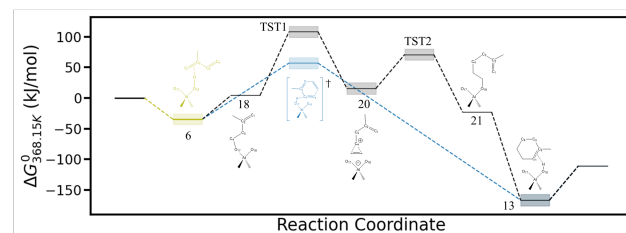

Fig. 10 The Gibbs free energy surface at 368.15 K of isoprene oligomerizing with ethene to form the C7 product (Black) and the DA cyloaddition reaction outlined in figure 6 (Blue). The shaded regions represent the thermodynamic limits defined by the harmonic and Free Translator approximations, with the state representing an average between those two limits.

(para-cycloadduct). Under the HO approximation with an identical temperature and reactant ratio (2:1 for dienophile:diene), our MKM predicted a STY of 0.01 ($mmol - C7/mmol - H + /hour$), with C7 being most selective and the catalytic flux being an order of magnitude larger than the gas-phase flux. Under the Free Translator approximation, the rates of product formation drop significantly; and the catalytic flux was an order of magnitude smaller than the gas-phase flux. The reason for this phenomenon is discussed later, but was ultimately due to the overprediction of the cycloadduct binding energies.

We would like to briefly emphasize that Bernardon et al. achieved upwards of 90% selectivity toward their most favourable cycloadduct (the para- regioisomer), whereas under identical conditions and using an identical reactant diene (isoprene), we only obtained 61% toward our most favourable cycloadduct (C7), and our most favourable C10 product was the meta- regioisomer

(C10-meta2). Such increased selectivity and preference toward the para- regioisomer by Bernardon et al. can be explained by the difference in functionality between our dienophiles. In particular, methyl-acrylate contains an electron withdrawing ester group, which is known to lower the HOMO/LUMO energy gap in normal electron demand DA reactions and increase the corresponding reaction rate. Additionally, such an explanation would support the larger STY observed by Bernardon et al.

For our reaction between isoprene (diene) and ethene (dienophile), we set our conditions at 368.15 K and 1 atm with an inlet reactant ratio of 4:1 (dienophile:diene). We chose these conditions because of the larger STY of 0.4 ($mmol - C7/mmol - H + /hour$), with the catalytic flux being 3400% larger than the gas-phase flux; which accounted for less than 4% toward product formation. In an effort to limit the possibility of side product formation, while maximizing our catalytic flux we chose not to deviate too far from the conditions of Bernardon et al. (See Figure S7 of the Supporting Information.) In a previous study[46], we concluded that the PBE(DFT-D2) functional overestimated the experimental heat of adsorption of ethene within H-ZSM5 by 20 (kJ/mol) at 195 K. To address how this discrepancy would impact our results, we ran our MKM under a destabilized reaction system where intermediates and TSTs which explicitly interact with the Brønsted acid site were destabilized by 20 (kJ/mol). The resulting catalytic flux became 7000% larger than the gas-phase flux, owing largely to the increased desorption rates of our products.

The results of our MKM are shown in Table 4, which include reactant conversion, product selectivity/yield, and surface coverage. Two results were listed for each quantity, corresponding to the HO and Free Translator approximations discussed in SI.I of the Supporting Information. Each case was run separately, keeping reactant conversion at approximately 1%. Only adsorbates with the most significant coverage were listed; but accounted for at least 99% of the surface species. The reaction network implemented within the MKM and its corresponding kinetic parameters are given within Figure S6 and Table S2 of the Supporting Information.

Under the HO approximation, the C7 product was most selective at 70% with respect to isoprene. Between the C10 products the meta isomers were favored, exhibiting at least 9% more selectivity relative to the para products. This preference is related to their intrinsic barriers being on average 7 (kJ/mol) smaller than for the para cycloadducts. Overall, the DA products dominated the surface, accounting for at least 93% of the coverage, with chemisorbed ethene and physisorbed *trans*-isoprene mostly accounting for the remainder. The most abundant surface intermediate (MASI) was the C10-para2 product, with a coverage of 60%. The C10-para2 product was also the most stable C10 cycloadduct, it had a DFT energy that was 11 (kJ/mol) more favourable than the other C10 products and a desorption barrier that was 11-27 (kJ/mol) larger than all other products.

Under the Free Translator approximation, there was a precipitous drop in reactant conversion and product yield among all cycloadducts. Furthermore, the selectivity toward C7 had substantially increased, while the selectivity for the C10 products had decreased. Surprisingly, the catalytic flux for the formation of all cycloadducts was reduced by two orders of magnitude relative to the HO approximation. For the C7 product in particular, the gas phase flux was an order of magnitude larger than its catalytic flux, implying that its selectivity is primarily the result of reactions occurring in the gas phase. Moreover, its smaller gas phase activation barrier (See S2 of the Supporting Information) relative to the formation of C10 products supports its large selectivity. The coverage of ethene and isoprene was also reduced, accounting for less than 0.01% of the surface species. On the other hand, each cycloadduct experienced an increase in coverage, now accounting for over 99% of the surface species. Consequently, it was determined that the desorption of products was rate limiting, being directly caused by the enhanced stability accrued by the Free Translator approximation. As intended, the Free Translator approximation serves as an upper-bound for the entropic freedom of the adsorbates, but likely overestimates the stability of our products and underestimates the rate.

The molecular surface area for translational entropy used within this study (200 x 600 pm) was derived by Moor et al.[56] for C2-C8 n-alkanes. The surface area was calculated with their physisorbed configurations having been oriented along the straight channel; with the Brønsted proton interacting with one of the carbon atoms. Unlike n-alkanes, no orientation of our cyclic products along the straight channel can afford such freedom. Moreover, the presence of Brønsted-π interactions for our products at the acid site (orientations shown in Figure 4) introduces enhanced stability relative to n-alkanes of an identical carbon number. We therefore presume that the actual entropy falls closer to the HO approximation; and have included a comparison among MKM results (See Table S2, Table S3, Table S4 in the Supporting Information) from the HO, Free Translator, and Free Translator/HO hybrid where only the product entropies were approximated by the HO. Ultimately, the results from the Free Translator/HO hybrid were largely similar to the HO, and we, therefore, performed the remainder of our kinetic analysis considering only the HO approximation.

3.4.1 Kinetic analysis

Table 5 shows the apparent order (derived by equation 10 of the Supporting Information) and inferred rate expression for each DA cycloaddition reaction under the HO approximation. The formation of C7 was found to be first order in ethene, following from its preference to react with the physisorbed *trans*-isoprene rather than acting as a competitive adosorbate that would otherwise saturate the surface. Suprisingly, the formation of C7 was found to be inhibited by isoprene, having a negative apparent order of approximately -0.5. As discussed in the next section, cycloadduct desorption was found to be rate limiting and ultimately the cause behind isoprene inhibiting C7 formation. The inferred rate expressions for C10 production were all essentially identical, being zero order with respecive to ethene, and approximately half order with respect to isoprene. The C10 cycloadducts are formed by the reaction between two isoprene molecules, justifying the zeroth order in ethene. Moreover, physisorbed *trans*-isoprene was the preffered adsorbate at the acid site, therefore ethene adsorption had little to no effect as a competitive adsorbate. The half-

adsorbate	Conversion %	Yield %	Selectivity %	Fractional Coverage
ethene	0.2(0.01)	-	-	$6.8 \times 10^{-2}(5.7 \times 10^{-7})$
isoprene	1.1(0.04)	-	-	$1.6 \times 10^{-3}(1.8 \times 10^{-6})$
C7	-	0.8(0.03)	69.9(97.7)	$2.0 \times 10^{-2}(6.2 \times 10^{-3})$
C10-para1	-	0.01(<0.001)	0.7(0.09)	$9.5 \times 10^{-3}(1.2 \times 10^{-2})$
C10-para2	-	0.1(<0.001)	10.3(0.79)	$6.0 \times 10^{-1}(6.6 \times 10^{-1})$
C10-meta1	-	0.01(<0.001)	1.0(0.08)	$4.1 \times 10^{-2}(5.1 \times 10^{-2})$
C10-meta2	-	0.2(<0.001)	18(1.4)	$2.6 \times 10^{-1}(2.8 \times 10^{-1})$

Table 4 The conversion, selectivity, and coverage (at 368.15 K and 1 atm) per adsorbate quantified from the MKM. The isoprene conversion included both isomers (*cis−* and *trans−*). The coverage for ethene and isoprene included their physisorbed, chemisorbed, and carbenium states on O17 and O16, including both isomers of isoprene (*cis−* and *trans−*). Free Translator quantities are housed within parenthesis

	n_{C2}	n_{C5}	Inferred rate expression
r_{C7}	0.93	-0.54	$\sim (k_{C7})p_{C2}p_{C5}^{-0.5}$
r_{C10P1}	-0.08	0.47	$\sim (k_{C10P1})p_{C5}^{0.5}$
r_{C10P2}	-0.08	0.47	$\sim (k_{C10P2})p_{C5}^{0.5}$
r_{C10M1}	-0.08	0.47	$\sim (k_{C10M1})p_{C5}^{0.5}$
r_{C10M2}	-0.08	0.47	$\sim (k_{C10M2})p_{C5}^{0.5}$

Table 5 The apparent order (n_i) under the HO approximation for each DA cycloaddition reaction with respect to ethene (C2) and isoprene (C5), as defined by equation 10 using the inferred rate expressions in the Supporting Information

order of isoprene in C10 production suggests that, much like in C7 production, the desorption of cycloadducts is also inhibitory. The apparent activation energy for the total consumption of isoprene under the HO approximation was 109 (kJ/mol), which suggests that the reaction can be further driven thermally. (See Figure S1 of Section SI.III)

3.4.2 Global sensitivity analysis

The degree of rate control (DORC) defined by Campbell[90,91] offers a robust approach toward finding the kinetically controlling steps in a reaction network. The notion behind this technique is to quantify the response of the overall reaction to a perturbation in the free energy of the TST or reaction intermediate and therefore the intrinsic barrier of that particular step. The outcome is a collection of quantities defining the enhancement/inhibition that each step within the network has on the overall rate. A limitation of this technique however, is that it only captures local sensitivities; since there are intrinsic errors in applying the DFT-D2 functional and uncertainty in calculating the entropy, we prefer a global estimate of sensitivities.

A variance-based global sensitivity analysis for catalytic reactions has recently been developed by Tian and Rangarajan[92], and we have applied their approach to our system. Although the formulation of this method is outside the scope of this paper, we summarize the resulting quantities and how they can be used to infer kinetic relationships. In particular, the individual influence of an elementary step or reaction intermediate "i" on the overall rate is defined by "S_i", while the combined influence between "i" with elementary step or reaction intermediate "j" is defined by "S_{ij}". The "S_{ij}" variable encapsulates the nonlinearity of the MKM, as well as the extent to which the instantaneous change

in the overall reaction rate with respect to parameter "i" (or "j") is dependent on the value of the other. In theory, the combined influence of every step and reaction intermediate within the network may be calculated ($S_{ijk...N}$), however this is typically not necessary and would require significant computational resources. Upon observing that the DA products dominate the surface coverage, we have limited our analysis to: 1) our catalyzed DA cycloaddition steps and the adsorption/desorption of their respective cycloadducts; 2) their adsorbed reactant/product intermediates (physisorbed ethene, isoprene, and each cycloadduct). The rate of isoprene consumption (limiting reactant) was defined as the overall rate, and the free energies of the TSTs and intermediates were perturbed to quantify the sensitivities. The perturbation range specified by the user has a significant impact on the resulting sensitivities, with small deviations from the nominal point encompassing local information (similar to DORC), while larger perturbations encompass global information, such as the correlation among parameters. It should be noted that while the DORC can be negative for some catalytic systems, the global sensitivities are always non-negative by definition.

Figure 11 shows the individual "S_i" and total "S_i^T" global sensitivities of the catalyzed DA cycloaddition reactions, their corresponding product adsorption steps, and their corresponding reaction intermediates under perturbation ranges from [-0.05, 0.05], [-5.0, 5.0], and [-7.5, 7.5] (kJ/mol) at 368.15 (K), 1 (atm) using the HO approximation. The "S_i^T" variable captures the net influence of parameter "i", including its contribution toward the other parameters; and therefore must always be larger than the individual contribution "S_i". Under small perturbations about the nominal point ([-0.5,0.5] (kJ/mol)), the sensitivities are qualitatively identical to the DORC. The overall reaction was most sensitive to the C7 DA cycloaddition step (R_{C7}^{DA}); this result is consistent with C7 being the most selective product and exhibiting the lowest relative Gibbs free energy difference ΔG_{rel}. Therefore, stabilizing the C7 TST would most influence the overall rate of this network. Following C7, the reaction rate was most sensitive to the formation and desorption of C10-para2 (R_{P2}^{DA}, R_{P2}^{ads}, I_{P2}), which also exhibited the most exergonic adsorption step among the cycloadducts, and largest surface coverage (60%) among all adsorbed species. Among these parameters, the overall rate was most sensitive to the stability of the C10-para2 intermediate (I_{P2}). This result coincides with the precipitous drop in catalytic flux and upsurge in C10-para2 coverage (97.7%) under the Free Translator approx-
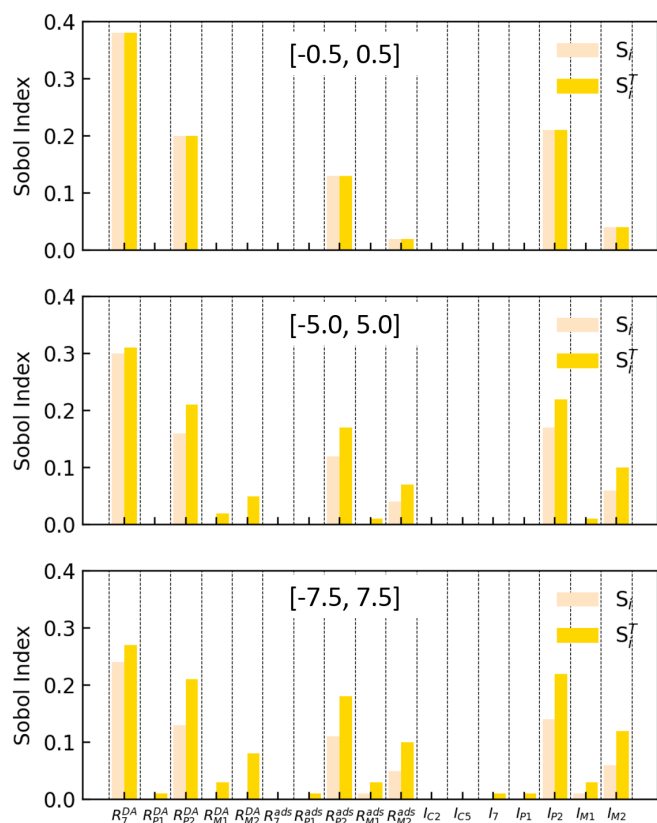
imation, implicating that destabilizing the adsorbed C10-para2 product would increase the catalytic rate. The remaining sensitivities were marginal; and included the rate of adsorption of C10-meta2 (R_{M2}^{ads}) and its adsorbed intermediate (I_{M2}). Similar to C10-para2, the rate was more sensitive to adsorbed C10-meta2, which was also the second most abundant surface intermediate (26%). Therefore in addition to C10-para2, the destabilization of the C10-meta2 adsorbate would increase the catalytic rate. As the range of allowed deviation is increased ([-5.0,5.0], [-7.5,7.5] (kJ/mol)), more parameters become important and the individual sensitivities of the C7, C10-para2, and C10-meta2 DA cycloaddition and adsorption steps/intermediates decrease, but the general rank of sensitivities remains unchanged. Moreover, we begin seeing that $S_i < S_i^T$, indicating that a combined contribution of multiple reactions steps and intermediate species affects the overall rate.

Figure 12 shows the heat map of S_{ij}, which can be thought of as a 2D correlation plot, where S_{ij} quantifies the extent to which the combination of parameters "i" and "j" influence the overall rate. The average magnitude of S_{ij} values progressively increase as the range is expanded from [-0.5, 0.5] to [-7.5, 7.5] (kJ/mol). This is consistent with S_i decreasing relative to S_i^T as the perturbation range is increased within Figure 11. The strongest correlations among the parameters are the DA cycloaddition step, adsorption step, and adsorbed intermediate of C10-para2 and of C10-meta2. Each of these parameters are kinetically related and consistent with the influence of C10-para2 and C10-meta2 on the overall rate. But apart from reinforcing our observations from Figure 11, the heatmap of Figure 12 shows that the formation of C7, formally the most influential independent parameter toward the reaction rate, is relatively uncorrelated with any species. This is also illustrated in Figure 11, where the difference between "S_i^T" and "S_i" are much smaller for C7 than for C10-para2 or C10-meta2. A possible explanation would be that C7 had the smallest ΔG_{rel}, such that its formation and desorption rates were at least an order of magnitude larger than any other cycloadduct (See Table S4 of the Supporting Information). Therefore perturbations to C7 significantly impact the overall reaction (rate of isoprene consumption) by increasing/decreasing the rate of C7 formation, but do not significantly impact other steps/intermediates. Additionally, the formation of C7 was found to faintly correlate with the formation of C10-meta2, which exhibited the smallest ΔG_{rel} and largest formation/desorption rate among the C10 products.

Fig. 11 Global sensitivity values S_i and S_i^T for each catalyzed reaction step "R" and adsorbed intermediate "I", where the "DA" and "ads" superscripts correspond to the DA cycloaddition and corresponding product cycloadduct adsorption steps: C7 (R_7, I_7), C10-para1 (R_{P1},I_{P1}) , C10-para2 (R_{P2},I_{P2}), C10-meta1 (R_{M1},I_{M1}), C10-meta2 (R_{M2},I_{M2}), and adsorbed reactants ethene (I_{C2}), isoprene (I_{C5}) at 368.15 (K) and 1 (atm) under the HO approximation for perturbation ranges ([-0.5,0.5] to [-7.5,7.5] (kJ/mol)).

3.5 Effect of confinement

The extent of zeolite catalysis depends upon the relative stability of adsorbed intermediates and their transition states. Under isothermal-isobaric conditions, the stability is explicitly defined by the Gibbs free energy, which can be deconstructed into contributions from the enthalpy and entropy. In our system, the enthalpy is mainly a measure of the Brønsted-π interactions at the acid site and dispersive (Van der Waals) interactions between the adosrbate and framework. By contrast, the entropy can be exemplified as a measure of the degrees of freedom lost upon the molecule adsorbing within the framework. Each of these quantities is dic-
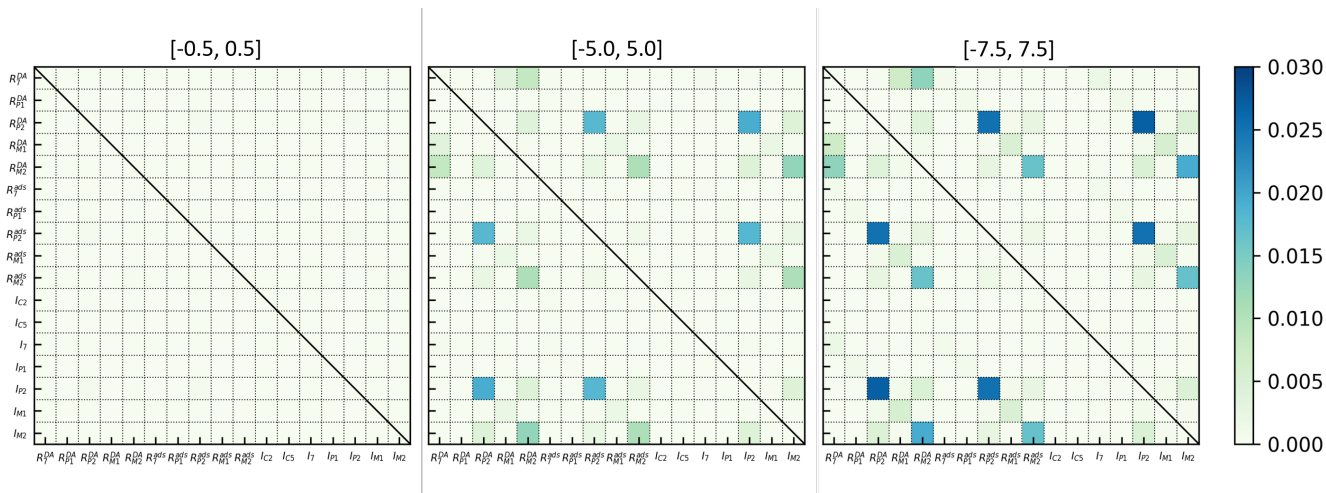
Fig. 12 Heat maps of S_{ij} values for each of the catalyzed DA reactions and corresponding adsorbed intermediates defined in figure 11 at 368.15 (K) and 1 (atm) for perturbation ranges ([-0.5,0.5] to [-7.5,7.5] (kJ/mol)). Note, the map is symmetric, such that $S_{ij} = S_{ji}$ and S_{ii} is not defined. As the parameter range is broadened, more S_{ij} values become significant.

tated by the extent of confinement, and in this section, we discuss its role in catalyzing the overall reaction. Specifically, we begin by showing how subtle changes in the enthalpy, entropy; and thereby confinement, effect the overall reaction. From the enthalpic perspective, we show that the long-range dispersive interactions between the adsorbate with the framework structure, rather than the Brønsted-π interactions at the acid site, are primarily responsible for the catalytic activity. Finally, we demonstrate how confinement can be leveraged to control the selectivity of our C7 product by varying the reactant inlet concentration ratio.

The effects of confinement have been shown to discriminate based on adsorbate size and shape. Namely, the enthalpy of adsorption for C2-C8 alkanes have shown to scale linearly with their carbon number.[56] Likewise, differences in the adsorption entropy between n-alkanes and their branched isomers have been shown to drive their separation in various zeolite frameworks.[93] To this extent, we examine the individual influence of each quantity on our reaction system. In Figure 13, we plot the reaction flux ratio (adsorbed-phase vs. unadsorbed gas-phase isoprene consumption) from our MKM against a span of temperatures. The local maximum found within Figure 13 a. is a consequence of the HO approximation. Specifically, as the temperature is increased, penalties to the Gibbs free energy of the form $T\Delta S$ become more significant. It is likely that the HO severely underpredicts the entropic freedom of adsorbates at high temperatures. We would like to emphasize that both, r_{ads} and r_{gas} continuously increase with temperature; but at higher temperatures, r_{ads} increases less rapidly than r_{gas} (See Figure S8 of the Supporting Information). In Figure 13 a., we have perturbed the enthalpy of each of our adsorbed species by $\pm$ 0.5 ((kJ/mol)/carbon-atom), replicating the effect that smaller and larger pores would have on the adsorbate stability respectively. Destabilizing our adsorbates by as little as 0.5 (kJ/mol) per carbon atom showed a substantial improvement ($\approx$ 6x) in the flux ratio for our nominal temperature. This result is consistent with the reaction being desorption lim-

ited by C10-para2 and C10-meta2, where destabilization of adsorbed states (and therefore increasing the rate of desorption) increases the overall rate of the reaction despite also increasing their relative reaction barriers. In Figure 13 b., we have incrementally increased the entropy of the adsorbed species from the HO to the Free Translator approximation, mimicking the effect of small and large pores respectively. Consistent with the MKM results under the Free Translator approximation (See section 3.4.1), the catalytic flux diminishes as the adsorbates gain entropic freedom, owing again to the reaction system being desorption limited. Figure 13 illustrates the considerable effects of confinement on the catalysis of our DA reactions. Namely, running this reaction within a framework which destabilizes the adsorbed species as little as 0.5 (kJ/mol) per carbon atom relative to HZSM-5, while limiting their entropic freedom to harmonic oscillations, may improve catalytic performance by almost an order of magnitude.

3.5.1 Energetic contributions

In this section we discuss the source of catalytic activity from the enthalpic perspective. Namely, we consider two primary sources for the enhanced stability of adsorbed species relative to their unadsorbed gas phase: 1)The Brønsted-π interactions at the acid site, 2) long-range dispersive interactions between the adsorbate and framework structure. The enthalpy of a molecule can be deconstructed into contributions from the electronic energy, zero point energy, and temperature corrections (See equation 3 of section SI.I in the Supporting Information). At our nominal condition the electronic energy is the most significant contributor toward the enthalpy; and it can be further deconstructed into Perdew–Burke-Ernzerhof (PBE)[43] and Grimme-D2 (dispersion)[45] energy contributions according to the following equation.

$$E_{Total} = E_{PBE} + E_{Disp} \tag{2}$$

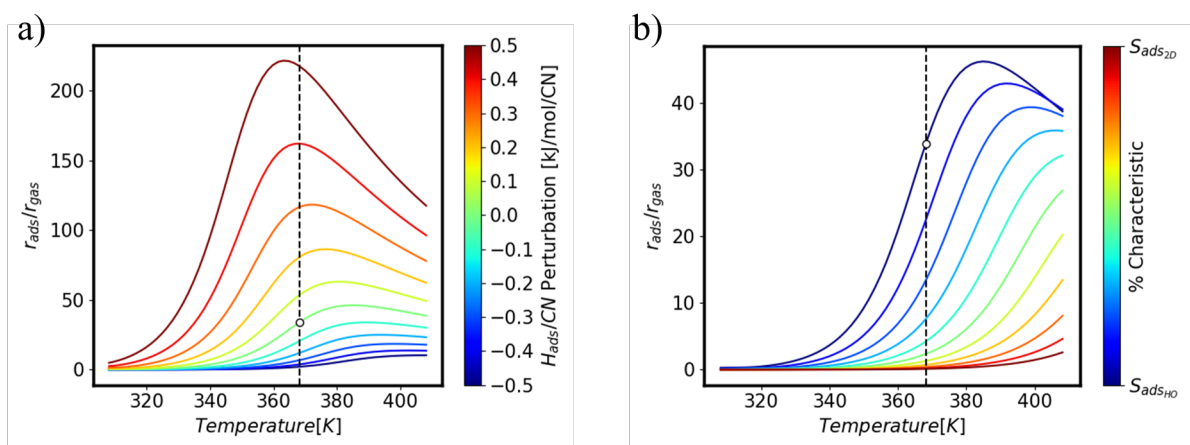Where "E_{Total}", "E_{PBE}", "E_{Disp}" represent the total, PBE, and

Fig. 13 Plots of the reaction flux ratios (adsorbed-phase vs. unadsorbed gas-phase isoprene consumption) against temperature, with a) Perturbed enthalpy of all adsorbed species scaled by the number of their carbon atoms, b) incremental (increments of 10%) increase of the entropic freedom of all adsorbed species between the HO (0%), to the Free Translator (100%) approximations. The dashed line with the white marker represents our nominal condition of 368.15 K.

Grimme-D2 energies respectively. A common drawback of GGA type functionals in the Kohn-sham formalism, including PBE, is the incapability of capturing long-range electron correlations responsible for Van der Waals (dispersion) interactions.[94–96] Nevertheless, PBE has proven reliable in predicting hydrogen bonded and ionic interactions.[97] The Grimme D2 energies naturally allows one to extract the dispersion contributions to the total energy. Applying equation 2 to the relative energy difference between the adsorbed TST and unadsorbed reactants "ΔE_{rel}" and unadsorbed gas-phase barriers "$\Delta E_{af(g)}$" from Figure 3, separates the energy differences into PBE and dispersion contributions. These deconstructed energies are plotted in Figure 14, with corresponding values listed in Table 6. The unadsorbed gas-phase and adsorbed phase reaction energies were plotted with solid line and dash-dot borders within Figure 14 respectively. Contributions from the PBE and dispersion corrections are represented by cross hatches and hatches respectively. We would like to emphasize that negative values for "ΔE_{rel}" and "$\Delta E_{af(g)}$" remain valid, and are a consequence of the large binding energy of the adsorbed reactants. The most significant observation from Figure 14 is that the differences in PBE energy barriers for the adsorbed and unadsorbed gas phase reactions are much smaller than the differences in Grimme-D2 energies. This suggests that the TSTs are mainly stabilized by the long-range van der Waals interactions from the framework (i.e confinement), rather than the interactions between the Brønsted proton and the π-bond of the TST. These results also suggest that a purely siliceous MFI type framework, one without a Brønsted acd site, should be capable in catalyzing these DA reactions.

3.5.2 Modulating selectivity

In this section, we demonstrate how the discriminating effects of confinement toward our DA reactions can be leveraged in controlling the catalytic product distribution by modulating the inlet reactant ratio. Figure 15 shows: 1) the selectivity of C7 cycloadduct and 2) the ratio of product formation rates (C7/C10),

Reaction	Adsorbed-Phase [(kJ/mol)]			Gas-Phase [(kJ/mol)]		
	ΔE_{rel}	ΔE_{disp}	ΔE_{PBE}	$\Delta E_{af(g)}$	ΔE_{disp}	ΔE_{PBE}
C7	-80	-123	44	53	-21	75
C10 − para1	-83	-183	100	52	-29	81
C10 − para2	-82	-182	100	60	-27	87
C10 − meta1	-89	-180	91	56	-29	86
C10 − meta2	-86	-171	85	57	-32	89

Table 6 The relative energy difference between the adsorbed TST and unadsorbed reactants "ΔE_{rel}", and unadsorbed gas-phase apparent barrier "$\Delta E_{af(g)}$" deconstructed into their corresponding PBE and dispersion energy contributions

as a function of the reactant feed ratio, as predicted by the MKM. For each plot, the catalytic flux was ensured to be at least an order of magnitude larger than its respective gas phase flux. The selectivity toward C7 can be defined by the ratio of product formation to isoprene consumption (r_{C7}/r_{C5}), as defined by equation 3. At high ethene partial pressures, the consumption of isoprene by the formation of C10 products diminishes relative to C7 formation, driving the selectivity toward unity. The selectivity toward C10 is also defined by equation 3; and is consistent with the plot of product formation rates as a function of partial pressure ratio in Figure 15 b. In particular, the ratio of inferred rate expressions for C7 against C10 (see table 5), produces a linear function with slope $\frac{1}{2}(k_{C7}/k_{C10})$ and a y-intercept of 0. This is replicated within Figure 15 b, suggesting that the selectivity defined within equation 3 is valid for C10 formation.

$$S(C7/C5) = \frac{k_{C7}\frac{p_{C2}}{\sqrt{p_{C5}}}}{k_{C7}\frac{p_{C2}}{\sqrt{p_{C5}}} + 2k_{C10}\sqrt{p_{C5}}}$$

(3)

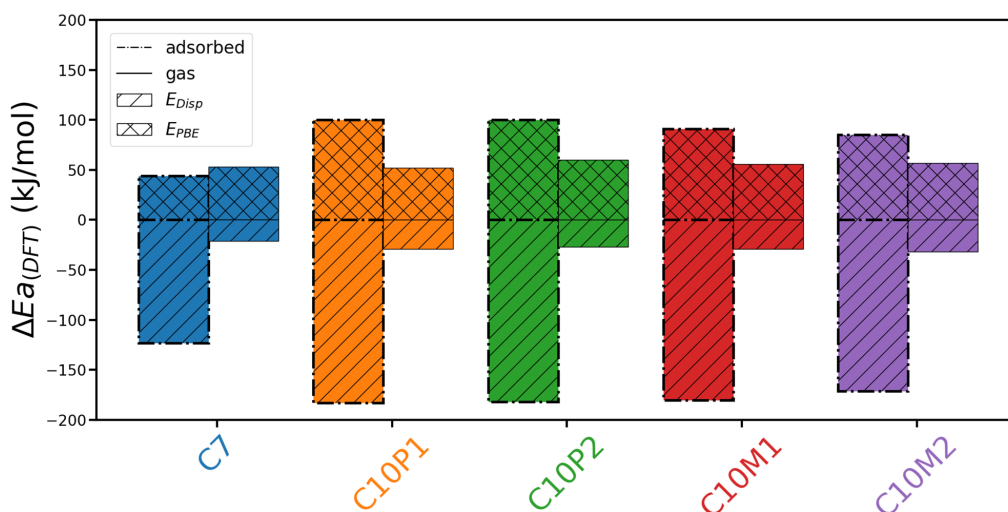$$S(C10/C5) = \frac{2k_{C10}\sqrt{p_{C5}}}{k_{C7}\frac{p_{C2}}{\sqrt{p_{C5}}} + 2k_{C10}\sqrt{p_{C5}}}$$

Fig. 14 The relative energy difference between the adsorbed TST and unadsorbed reactants "ΔE_{rel}" and apparent barrier "$\Delta E_{af(g)}$" for the catalyzed (alternating line-dot border) and gas phase (straight-line border) DA cycloaddition reactions outlined within Figure 6. The DFT energy has been separated between the Perdew-Wang-Ernzerhof (PBE)[43] energy (cross-hatch filled) of the exchange correlation functional and the Grimme-D2[44,45] dispersion correction energy (line-hatch filled). The differences between the adsorbed and unadsorbed gas phase PBE energies are small for each reaction relative to the differences between the adsorbed and unadsorbed gas phase dispersion energies are large for each reaction.
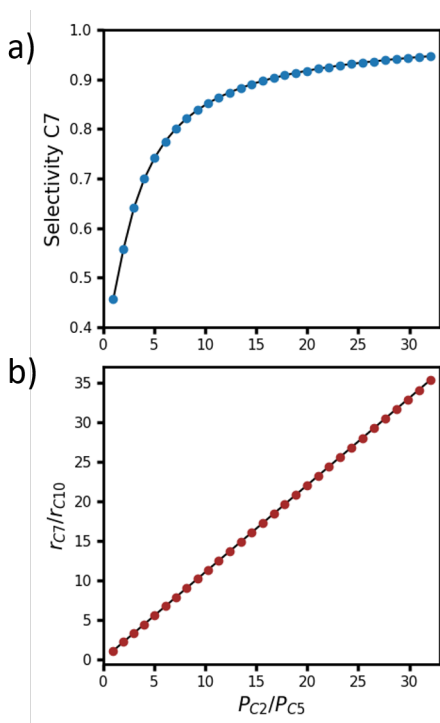

Fig. 15 Plots of: a) the Selectivity, predicted by the MKM, of C7, and b) the ratio of C7 to C10 reaction rates, as a function of reactant ratio: (ethene/isoprene), otherwise (dienophile/diene).

4   Conclusions

We performed a mechanistic study on the DA cycloaddition reactions between ethene and isoprene within H-ZSM5 using dispersion corrected DFT calculations. Temperature corrections were implemented using the HO and Free Translator approximations, offering a lower and upped bound on our MKM results respectively. The product cycloadducts produced a range of cyclic regio-isomers, which were the basis for studying how zeolite confinement would impact their stability and selectivity based on size and shape. The products included a smaller C7 cycloadduct produced from the coupling between ethene and isoprene, as well as four larger C10 cycloadducts produced by the coupling between two isoprene molecules. These corresponding C10 products were categorized based on their para- and meta- regiochemistry.

Our DFT results have shown adsorbate configurations and adsorption values consistent with available works. It was found that the DA cycloaddition reactions within H-ZSM5 were catalyzed with respect to their gas phase reactions; but with C10-para products having on average 7 (kJ/mol) larger intrinsic barriers than the C10-meta products. The driver for catalysis was determined to be the stability of the DA TSTs caused by their favourable van der Waals interactions with the framework (i.e confinement).

Oligomerization and cyclization mechanisms were also considered as potentially competitive pathways. In particular, we have investigated the chemisorption of our olefins via the formation of covalent alkoxide bonds with the oxygen atoms of the framework. Chemisorbed ethene was found to be thermodynamically competitive with physisorbed *trans*-isoprene; but its intrinsic barrier rendered it kinetically unfavourable. A subsequent cyclization pathway for C7 formation was also investigated, beginning with olgiomerization ocurring between a primary isoprene alkoxide with co-adsorbed ethene and concluding with dehydrogenation of a six-membered cyclic product. However, this pathway was found

to be both kinetically and thermodynamically unfavourable relative to DA cycloaddition.

Our DFT results were fed into a differential CSTR based MKM, with conditions replicated from an experimental work studying the DA reactions between isoprene and methyl-acrylate.[33] Our model was able to capture similar site time yields to experiments; but to enhance our catalytic flux we settled upon a larger reactant feed ratio and temperature. Under the Free Translator approximation, the gas phase flux for the formation of C7 was found to be an order of magnitude larger than its respective catalytic flux. Under this approximation, the desorption of cycloadducts was found to be rate limiting, with the Free Translator approximation presumably under-estimating the entropic loss of adsorbed intermediates. Consequentially, combining the Free Translator approximation with the HO approximation for adsorbed cycloadducts produced largely similar MKM results to the HO approximation. Further analysis using the HO approximation has shown appreciable selectivity toward the C7 product (70%); and this approximation was used for the remainder of our analysis.

The apparent order for the formation of our C7 product was found to be first order in ethene but negative half order with respect to isoprene, suggesting that isoprene inhibits C7 formation. The apparent orders for formation of our C10 products were largely similar, all being zero order with respect to ethene; but half order with respect to isoprene. A global sensitivity analysis was implemented on our MKM, which showed that isoprene consumption (limiting reactant) was most sensitive to 1) the formation of C7, 2) the DA cycloaddition and adsorption steps of C10-para2 and C10-meta2 and their corresponding adsorbed state (the two most abundant surface intermediates). Surprisingly, the formation of C7 was largely uncorrelated with any other parameters, despite contributing the greatest individual influence on the overall rate. It was posited that because C7 had the smallest ΔG_{rel}, with formation and desorption rates at least an order of magnitude larger than the other cycloadducts, that perturbations to the C7 TST resulted in significant consumption of isoprene but otherwise insignificant contributions to the other steps.

Author Contributions

S.R.'s contribution to this study include: Conceptualization, Funding acquisition, Project administration, Resources, Supervision, Writing – review & editing. C.R.'s contribution to this study include: Data curation, Formal analysis, Investigation, Methodology, Software, Validation, Visualization, Writing – original draft.

Conflicts of interest

There are no conflicts to declare.

Acknowledgements

Notes and references

1 A. Corma, *Zeolites: Facts, Figures, Future Part A - Proceedings of the 8th International Zeolite Conference*, Elsevier, 1989, vol. 49, pp. 49–67.

2 A. Corma, *Chem. Rev.*, 1995, **95**, 559–614.

3 Z. Jie, C. Yu, C. Yuanjun, Z. Huaqun, Y. Wang and F. Wei, *Journal of Chemical Industry and Engineering (China)*, 2010, **61**,.

4 S. Ilias and A. Bhan, *ACS Catalysis*, 2013, **3**, 18–31.

5 V. R. Choudhary, S. K. Jana and B. P. Kiran, *Catalysis Letters*, 1999, **59**, 217–219.

6 M. Linares, C. Vargas, A. García, C. Ochoa-Hernández, J. Čejka, R. A. García-Muñoz and D. P. Serrano, *Catal. Sci. Technol.*, 2017, **7**, 181–190.

7 S. Sartipi, K. Parashar, M. Makkee, J. Gascon and F. Kapteijn, *Catal. Sci. Technol.*, 2013, **3**, 572–575.

8 L.-H. Chen, M.-H. Sun, Z. Wang, W. Yang, Z. Xie and B.-L. Su, *Chemical Reviews*, 2020, **120**, 11194–11294.

9 E. G. Derouane, in *Confinement Effects in Sorption and Catalysis by Zeolites*, ed. D. Barthomeuf, E. G. Derouane and W. Hölderich, Springer US, Boston, MA, 1990, pp. 225–239.

10 B. Smit and T. L. M. Maesen, *Nature*, 2008, **451**, 671–678.

11 A. Bhan and E. Iglesia, *Accounts of Chemical Research*, 2008, **41**, 559–567.

12 G. Noh, Z. Shi, S. I. Zones and E. Iglesia, *Journal of Catalysis*, 2018, **368**, 389–410.

13 S. P. Crossley, D. E. Resasco and G. L. Haller, *Journal of Catalysis*, 2019, **372**, 382–387.

14 R. Y. Rohling, I. C. Tranca, E. J. M. Hensen and E. A. Pidko, *The Journal of Physical Chemistry C*, 2018, **122**, 14733–14743.

15 Y. Liu, L. Annamalai and P. Deshlahra, *The Journal of Physical Chemistry C*, 2019, **123**, 28168–28191.

16 L. Annamalai, Y. Liu, S. Ezenwa, Y. Dang, S. L. Suib and P. Deshlahra, *ACS Catalysis*, 2018, **8**, 7051–7067.

17 H. S. Khanna, A. Mirich, A. Twombly, Y. Dang, A. Shirazi-Amin, I. Perera, Y. Liu, L. F. Posada, P. Deshlahra and S. L. Suib, *Applied Catalysis A: General*, 2022, **635**, 118557.

18 D. Chakraborty and P. K. Chattaraj, *Journal of Computational Chemistry*, 2018, **39**, 151–160.

19 J.-A. Funel and S. Abele, *Angewandte Chemie International Edition*, 2013, **52**, 3822–3863.

20 A. E. Settle, L. Berstis, N. A. Rorrer, Y. Roman-Leshkóv, G. T. Beckham, R. M. Richards and D. R. Vardon, *Green Chem.*, 2017, **19**, 3468–3492.

21 N. Nikbin, P. T. Do, S. Caratzoulas, R. F. Lobo, P. J. Dauenhauer and D. G. Vlachos, *Journal of Catalysis*, 2013, **297**, 35–43.

22 P. T. M. Do, J. R. McAtee, D. A. Watson and R. F. Lobo, *ACS Catalysis*, 2013, **3**, 41–46.

23 K. N. Houk, J. Gonzalez and Y. Li, *Accounts of Chemical Research*, 1995, **28**, 81–90.

24 M. Yoshizawa, M. Tamura and M. Fujita, *Science*, 2006, **312**, 251–254.

25 H. Yamamoto and K. Futatsugi, *Angewandte Chemie International Edition*, 2005, **44**, 1924–1942.

26 A. Wassermann, *J. Chem. Soc.*, 1942, 618–621.

27 P. Yates and P. Eaton, *Journal of the American Chemical Society*, 1960, **82**, 4436–4437.

28 A. Corma, S. Iborra and A. Velty, *Chemical Reviews*, 2007, **107**, 2411–2502.

29 C. L. Williams, C.-C. Chang, P. Do, N. Nikbin, S. Caratzoulas, D. G. Vlachos, R. F. Lobo, W. Fan and P. J. Dauenhauer, *ACS Catalysis*, 2012, **2**, 935–939.

30 N. Nikbin, S. Feng, S. Caratzoulas and D. G. Vlachos, *The Journal of Physical Chemistry C*, 2014, **118**, 24415–24424.

31 R. Y. Rohling, E. Uslamin, B. Zijlstra, I. C. Tranca, I. A. W. Filot, E. J. M. Hensen and E. A. Pidko, *ACS Catalysis*, 2018, **8**, 760–769.

32 R. Y. Rohling, I. C. Tranca, E. J. M. Hensen and E. A. Pidko, *ACS Catalysis*, 2019, **9**, 376–391.

33 C. Bernardon, B. Louis, V. Bénéteau and P. Pale, *ChemPlusChem*, 2013, **78**, 1134–1141.

34 M. den Hollander, M. Wissink, M. Makkee and J. Moulijn, *Applied Catalysis A: General*, 2002, **223**, 85 – 102.

35 X. Zhu, S. Liu, Y. Song and L. Xu, *Applied Catalysis A: General*, 2005, **288**, 134 – 142.

36 J. Buchanan, *Catalysis Today*, 2000, **55**, 207 – 212.

37 *Database of Zeolite Structures*, `http://www.iza-structure.org/databases/`, 2012, Accessed: 2020-12-07.

38 A. Ghorbanpour, J. D. Rimer and L. C. Grabow, *Catalysis Communications*, 2014, **52**, 98 – 102.

39 Y. Zhang, J. Yu, Y.-H. Yeh, R. J. Gorte, S. Rangarajan and M. Mavrikakis, *The Journal of Physical Chemistry C*, 2015, **119**, 28970–28978.

40 G. Kresse and J. Furthmüller, *Computational Materials Science*, 1996, **6**, 15 – 50.

41 G. Kresse and J. Furthmüller, *Phys. Rev. B*, 1996, **54**, 11169–11186.

42 G. Kresse and D. Joubert, *Phys. Rev. B*, 1999, **59**, 1758–1775.

43 J. P. Perdew, K. Burke and M. Ernzerhof, *Phys. Rev. Lett.*, 1996, **77**, 3865–3868.

44 S. Grimme, *Journal of Computational Chemistry*, 2006, **27**, 1787–1799.

45 S. Grimme, J. Antony, S. Ehrlich and H. Krieg, *The Journal of Chemical Physics*, 2010, **132**, 154104.

46 Y.-H. Yeh, C. Rzepa, S. Rangarajan and R. J. Gorte, *Microporous and Mesoporous Materials*, 2019, **284**, 336 – 342.

47 G. Henkelman, B. P. Uberuaga and H. Jónsson, *The Journal of Chemical Physics*, 2000, **113**, 9901–9904.

48 C. M. Nguyen, B. A. De Moor, M.-F. Reyniers and G. B. Marin, *The Journal of Physical Chemistry C*, 2011, **115**, 23831–23847.

49 B. C. Bukowski, J. S. Bates, R. Gounder and J. Greeley, *Journal of Catalysis*, 2018, **365**, 261–276.

50 B. A. De Moor, A. Ghysels, M.-F. Reyniers, V. Van Speybroeck, M. Waroquier and G. B. Marin, *Journal of Chemical Theory and Computation*, 2011, **7**, 1090–1101.

51 K. De Wispelaere, L. Vanduyfhuys and V. Van Speybroeck, *Modelling and Simulation in the Science of Micro- and Meso-Porous Materials*, Elsevier, 2018, pp. 189–228.

52 C. T. Campbell and J. R. V. Sellers, *Journal of the American Chemical Society*, 2012, **134**, 18109–18115.

53 P. J. Dauenhauer and O. A. Abdelrahman, *ACS Central Science*, 2018, **4**, 1235–1243.

54 B. A. De Moor, M.-F. Reyniers, M. Sierka, J. Sauer and G. B. Marin, *The Journal of Physical Chemistry C*, 2008, **112**, 11796–11812.

55 B. A. De Moor, M.-F. Reyniers and G. B. Marin, *Phys. Chem. Chem. Phys.*, 2009, **11**, 2939–2958.

56 B. A. De Moor, M.-F. Reyniers, O. C. Gobin, J. A. Lercher and G. B. Marin, *The Journal of Physical Chemistry C*, 2011, **115**, 1204–1219.

57 S. Li, O. A. Abdelrahman, G. Kumar, M. Tsapatsis, D. G. Vlachos, S. Caratzoulas and P. J. Dauenhauer, *ACS Catalysis*, 2019, **9**, 10279–10293.

58 T. Baba, N. Komatsu, Y. Ono and H. Sugisawa, *The Journal of Physical Chemistry B*, 1998, **102**, 804–808.

59 V. Kazansky, *Catalysis Today*, 1999, **51**, 419 – 434.

60 J. F. Haw, J. B. Nicholas, T. Xu, L. W. Beck and D. B. Ferguson, *Accounts of Chemical Research*, 1996, **29**, 259–267.

61 A. Tkatchenko and M. Scheffler, *Phys. Rev. Lett.*, 2009, **102**, 073005.

62 S. N. Steinmann and C. Corminboeuf, *The Journal of Chemical Physics*, 2011, **134**, 044117.

63 S. N. Steinmann and C. Corminboeuf, *Journal of Chemical Theory and Computation*, 2011, **7**, 3567–3577.

64 M. Dion, H. Rydberg, E. Schröder, D. C. Langreth and B. I. Lundqvist, *Phys. Rev. Lett.*, 2004, **92**, 246401.

65 G. Román-Pérez and J. M. Soler, *Phys. Rev. Lett.*, 2009, **103**, 096102.

66 K. Lee, E. D. Murray, L. Kong, B. I. Lundqvist and D. C. Langreth, *Phys. Rev. B*, 2010, **82**, 081101.

67 A. Bhan, Y. V. Joshi, W. N. Delgass and K. T. Thomson, *The Journal of Physical Chemistry B*, 2003, **107**, 10476–10487.

68 C. M. Nguyen, B. A. De Moor, M.-F. Reyniers and G. B. Marin, *The Journal of Physical Chemistry C*, 2012, **116**, 18236–18249.

69 V. Nieminen, M. Sierka, D. Y. Murzin and J. Sauer, *Journal of Catalysis*, 2005, **231**, 393 – 404.

70 P. Cnudde, K. De Wispelaere, J. Van der Mynsbrugge, M. Waroquier and V. Van Speybroeck, *Journal of Catalysis*, 2017, **345**, 53 – 69.

71 A. G. Stepanov, M. V. Luzgin, V. N. Romannikov, V. N. Sidelnikov and E. A. Paukshtis, *Journal of Catalysis*, 1998, **178**, 466–477.

72 M. N. Mazar, S. Al-Hashimi, A. Bhan and M. Cococcioni, *The*

Journal of Physical Chemistry C, 2012, **116**, 19385–19395.

73 A. G. Stepanov, M. V. Luzgin, V. N. Romannikov, V. N. Sidelnikov and E. A. Paukshtis, *Journal of Catalysis*, 1998, **178**, 466 – 477.

74 M. C. Grady and R. J. Gorte, *The Journal of Physical Chemistry*, 1985, **89**, 1305–1308.

75 S. Vernuccio, E. E. Bickel, R. Gounder and L. J. Broadbelt, *ACS Catalysis*, 2019, **9**, 8996–9008.

76 A. Bhan, S.-H. Hsu, G. Blau, J. M. Caruthers, V. Venkatasubramanian and W. N. Delgass, *Journal of Catalysis*, 2005, **235**, 35–51.

77 M. Vandichel, D. Lesthaeghe, J. V. der Mynsbrugge, M. Waroquier and V. Van Speybroeck, *Journal of Catalysis*, 2010, **271**, 67–78.

78 Y. V. Joshi and K. T. Thomson, *Journal of Catalysis*, 2005, **230**, 440 – 463.

79 S. Svelle, S. Kolboe and O. Swang, *The Journal of Physical Chemistry B*, 2004, **108**, 2953–2962.

80 W. Shen, *Microporous and Mesoporous Materials*, 2017, **247**, 136–144.

81 M. N. Mazar, S. Al-Hashimi, M. Cococcioni and A. Bhan, *The Journal of Physical Chemistry C*, 2013, **117**, 23609–23620.

82 M. Sierka and J. Sauer, *The Journal of Physical Chemistry B*, 2001, **105**, 1603–1613.

83 E. M. Evleth, E. Kassab, H. Jessri, M. Allavena, L. Montero and L. R. Sierra, *The Journal of Physical Chemistry*, 1996, **100**, 11368–11374.

84 A. Rigby and M. Frash, *Journal of Molecular Catalysis A: Chemical*, 1997, **126**, 61–72.

85 V. Kazansky, *Catalysis Today*, 1999, **51**, 419–434.

86 Y. Chu, B. Han, A. Zheng and F. Deng, *The Journal of Physical Chemistry C*, 2012, **116**, 12687–12695.

87 D. Gleeson, *Journal of Chemometrics*, 2008, **22**, 372–377.

88 M. Boronat and A. Corma, *Applied Catalysis A: General*, 2008, **336**, 2–10.

89 T. Demuth, X. Rozanska, L. Benco, J. Hafner, R. van Santen and H. Toulhoat, *Journal of Catalysis*, 2003, **214**, 68–77.

90 C. T. Campbell, *ACS Catalysis*, 2017, **7**, 2770–2779.

91 C. Stegelmann, A. Andreasen and C. T. Campbell, *Journal of the American Chemical Society*, 2009, **131**, 8077–8082.

92 H. Tian and S. Rangarajan, *ACS Catalysis*, 2020, **10**, 13535–13542.

93 J. F. M. Denayer, R. A. Ocakoglu, I. C. Arik, C. E. A. Kirschhock, J. A. Martens and G. V. Baron, *Angewandte Chemie International Edition*, 2005, **44**, 400–403.

94 P. Hobza, J. šponer and T. Reschel, *Journal of Computational Chemistry*, 1995, **16**, 1315–1325.

95 M. J. Allen and D. J. Tozer, *The Journal of Chemical Physics*, 2002, **117**, 11113–11120.

96 S. Kristyán and P. Pulay, *Chemical Physics Letters*, 1994, **229**, 175–180.

97 M. Ernzerhof and G. E. Scuseria, *The Journal of Chemical Physics*, 1999, **110**, 5029–5036.